1   **Distribution Shapes Govern the Discovery of Predictive Models for Gene Regulation**

2

3   Running Title: **Predicting Transcription Dynamics**

4

5   Brian E. Munsky[1,2*], Guoliang Li[3], Zachary R. Fox[2], Douglas P. Shepherd[6], Gregor Neuert[3-5,*]

6

7   [1]Keck Scholar, Department of Chemical and Biological Engineering, Colorado State University,
8   Fort Collins, CO 80523, USA

9

10 [2]School of Biomedical Engineering, Colorado State University, Fort Collins, CO 80523, USA

11

12 [3]Department of Molecular Physiology and Biophysics, School of Medicine, Vanderbilt
13 University, Nashville, TN, 37232, USA

14

15 [4]Department of Biomedical Engineering, School of Engineering, Vanderbilt University,
16 Nashville, TN, 37232, USA

17

18 [5]Department of Pharmacology, School of Medicine, Vanderbilt University, Nashville, TN,
19 37232, USA

20

21 [6]Department of Physics, Pediatric Heart Lung Center, and Department of Pediatrics
22 University of Colorado Denver, Denver, CO 80217

23

24 [*]Senior authors to whom correspondence should be addressed
25 E-mail: munsky@colostate.edu; gregor.neuert@vanderbilt.edu

26

27 Keywords: modeling, prediction, quantitative, single-cell, transcription

28

29 Final Character Count including references (6,435), captions (4,627), title page, materials and
30 methods (16,319), and spaces): 47,664

31

32 **Significance Statement**
33 Systems biology seeks to combine experiments with computation to predict complex biological
34 behaviors. However, despite tremendous data and knowledge, most biological models make
35 terrible predictions. By analyzing single-cell-single-molecule measurements of mRNA in yeast
36 during stress response, we explore how prediction accuracy is controlled by experimental
37 distributions shapes. We find that asymmetric data distributions, which arise in measurements of
38 positive quantities, can cause standard modeling approaches to yield excellent fits but make
39 meaningless predictions. We demonstrate advanced computational tools that solve this dilemma
40 and achieve predictive understanding of many spatiotemporal mechanisms of transcription
41 control including RNA polymerase initiation and elongation and mRNA accumulation, transport
42 and decay. Our approach extends to any discrete dynamic process with rare events and
43 realistically limited data.

44

45

46

47

48   **Abstract:** Despite substantial experimental and computational efforts,
49   mechanistic modeling remains more predictive in engineering than in systems
50   biology. The reason for this discrepancy is not fully understood. Although
51   randomness and complexity of biological systems play roles in this concern, we
52   hypothesize that significant and overlooked challenges arise due to specific
53   features of single-molecule events that control crucial biological responses. Here
54   we show that modern statistical tools to disentangle complexity and stochasticity,
55   which assume normally distributed fluctuations or enormous datasets, don't apply
56   to the discrete, positive, and non-symmetric distributions that characterize
57   spatiotemporal mRNA fluctuations in single-cells. We demonstrate an alternate
58   approach that fully captures discrete, non-normal effects within finite datasets. As
59   an example, we integrate single-molecule measurements and these advanced
60   computational analyses to explore Mitogen Activated Protein Kinase induction of
61   multiple stress response genes. We discover and validate quantitatively precise,
62   reproducible, and predictive understanding of diverse transcription regulation
63   mechanisms, including gene activation, polymerase initiation, elongation, mRNA
64   accumulation, spatial transport, and degradation. Our model-data integration
65   approach extends to any discrete dynamic process with rare events and
66   realistically limited data.

67   The ultimate goal of modeling is to integrate quantitative data to understand, predict, or control
68   complex processes. Useful models may be discovered through mechanistic or statistical
69   approaches, but success is always limited by the quantity and quality of data and the rigor of
70   comparison between models and experiments. These issues are largely solved in engineering,
71   where computer analyses routinely enable the design of extraordinarily complex systems. Many
72   would argue that predictive modeling in biology is far behind this capability due to limited
73   experimental data, inescapable randomness or noise, and overwhelming biological complexity.
74   These concerns have driven rapid single-cell experimental and computational advances, which
75   have enabled measurement and modeling of individual biomolecules (i.e., DNA, RNA, and
76   protein) in single cells with outstanding spatiotemporal resolution[1-12]. Such experiments have
77   allowed the characterization of many intriguing aspects of biological complexity and variation[13],
78   while capturing these phenomena with stochastic gene regulation models has improved
79   understanding of mechanisms and their parameters[14-18].

81   Despite experimental and computational advances, most biological models still underperform
82   expectations. While it is tempting to attribute this failure to "poor models" or "insufficient data,"
83   an alternative and often overlooked explanation is that combinations of sufficient data and good
84   models may fail because they haven't been integrated properly. Many standard engineering
85   techniques exist to integrate models with continuous-valued data, but unlike most engineered
86   systems, biological fluctuations are dominated by *discrete* events. A single molecule of DNA,
87   RNA, or protein can change the fate of an organism[19-22]. The resulting positive and discrete
88   distributions violate the most basic assumption of most model inference approaches (i.e., that
89   measurement errors are continuous Gaussian random variables). Moreover, this violation is
90   compounded by the fact that datasets for single-cell imaging and sequencing are usually too
91   small to invoke the central limit theorem (CLT). Consequently, standard data-model integration
92   procedures can fail dramatically. We hypothesize that more exact treatment of discrete biological
93   fluctuations could solve the data-model integration dilemma and enable precise quantitative
94   predictions.

96   To test this hypothesis, we explore the effects of experimental data distribution shapes on the
97   uncertainty, bias, and resulting predictive capabilities of single-cell gene regulation models. We
98   examine the evolutionary conserved Stress Activated Protein Kinase (p38 / Hog1 SAPK) signal
99   transduction pathway (Figs. 1 and S1), and we quantify its control of transcription mechanisms
100   including RNA polymerase transcription initiation and elongation on target genes as well as
101   mature mRNA export and degradation in *Saccharomyces cerevisiae* during adaptation to hyper-
102   osmotic shock (Fig. 1A)[23]. We quantify the number of individual mRNA primary transcripts at
103   the site of transcription, in the nucleus, and in the cytoplasm for multiple genes using single-
104   molecule fluorescence *in situ* hybridization (smFISH) (Fig. 1B,C)[1,2]. We collect high-resolution
105   data from more than 65,000 cells, and we quantify single-cell spatiotemporal mRNA
106   distributions that are demonstrably non-normal and non-symmetric (Figs. S2-S3). For such
107   distributions, huge data sets would be needed to justify application of the CLT as we discuss
108   below. We use computational analyses to integrate these data with a discrete stochastic
109   spatiotemporal model[24] (Fig. 1A), and we show how different computational analyses of the
110   *same experimental data* and *same models* can yield vastly different parameter biases and
111   uncertainties which cause predictive accuracy to vary by many orders of magnitude (Fig. 1D).
112

113   We discover that standard single-cell modeling approaches, which assume continuous and
114   normally distributed fluctuations *or* enough data to invoke the CLT[24], are not always valid to
115   interpret finite datasets for single-cell transcription responses. We find that these standard
116   approaches can yield surprising errors and poor predictions (Fig. 1D), especially when mRNA
117   expression is very low. In contrast, we show that improved computational analyses of full single-
118   cell RNA distributions can yield far more precisely constrained, less biased, and more
119   reproducible models (Fig. 1D). We also discover new and valuable information contained in the
120   intracellular spatial locations of RNA (Figs. 1B, S4-S5), enabling quantitative predictions for
121   novel dynamics of gene regulation, including transcription initiation and elongation rates,
122   fractions of actively transcribing cells, and the average number and distribution of polymerases
123   per active transcription site, which could not otherwise be measured simultaneously in
124   endogenous cell populations (Figs. 1D, 4).

125

126   **Results**

127

128   Under osmotic stress, the high osmolarity glycerol kinase, Hog1, is phosphorylated and
129   translocated to the nucleus, where it activates several hundred genes[23]. For two of these genes
130   (*STL1*, a glycerol proton symporter of the plasma membrane and *CTT1*, the Cytosolic catalase
131   T), we quantified transcription at single-molecule and single-cell resolution (Figs. 1B,C, S2, and
132   S3), at temporal resolutions of one to five minutes, at two osmotic stress conditions (0.2M and
133   0.4M NaCl), and in multiple biological replicas. We built histograms to quantify the marginal
134   and joint distributions of the nuclear and cytoplasmic mRNA (Figs. 2D,E and S2-S5).

135

136   We extended a bursting gene expression model[14,25] to account for transcriptional regulation and
137   spatial localization of mRNA (Fig. 1A)[24]. We considered four approaches to fit this model to
138   gene transcription data: First, we used exact analyses of the first moments (i.e., population
139   means) of mRNA levels as functions of time. Second, we added exact analyses of the second
140   moments (i.e., variances and covariances). Third, we extended the moments analyses to include
141   the third and fourth moments. Finally, we used the finite state projection (FSP[26]) approach to
142   compute the full joint probability distributions for nuclear and cytoplasmic mRNA. *All four*
143   *approaches provide exact solutions of the same model*, but at different levels of statistical
144   detail[24]. We used each analysis to compute the likelihood that the measured mRNA data would
145   match the model, and we maximized this likelihood[24]. As was the case for previous studies[17,27],
146   we note that the moments-based likelihood computations assume either normally distributed
147   deviations (first and second methods) *or* sufficiently large sample sizes such that the moments
148   can be captured by a normal distribution as guaranteed by the CLT (third method)[24]. In contrast,
149   the FSP approach (fourth method) makes no assumptions on the distribution shape and has no
150   requirement for large sample sizes.

151

152   *Different exact analyses of the same model and same data yield dramatically different results.*
153   The four likelihood definitions were maximized by different parameter combinations (Tables S3
154   and S4), and the fit and prediction results are compared to the measured mean, variance, ON-
155   fraction (i.e., fraction of cells with more than 3 mRNA / cell), and distributions versus time for
156   *STL1* and *CTT1* (Figs. 2, S2, and S3). The different analyses used the same model, and they were
157   fit to the exact same experimental data, but they yielded dramatically different results. When
158   identified using the average mRNA dynamics (Fig. 2A, left), the model failed to match the

159   variance, ON-fractions, or distributions of the process (Fig. 2B-E, left). Fitting the response
160   means and variances simultaneously (Fig. 2A-B, center) failed to predict the ON-fractions or
161   probability distributions (Fig. 2C-E, center). In contrast, parameter estimation using the full
162   probability distribution (Fig. 2, right column and Figs. S2 and S3) matched all measured
163   statistics. Importantly, key parameters identified using the FSP approach agree well with
164   previous studies[18], such as *STL1* and *CTT1* mRNA transcription and degradation rates. This
165   agreement indicates strong reproducibility of both experiments and analyses (Tables S3 and S4)
166   and provides more confident predictions for new transcriptional mechanisms as discussed below.
167   In contrast, the moment-based analyses overestimated these rates by multiple orders of
168   magnitude.
169
170   *Standard modeling identification procedures fail due to bias in moment estimation.* We
171   considered three explanations for the failure of moment-based parameter estimation approaches:
172   (i) the model parameters could be unidentifiable from the considered moments; (ii) the
173   parameters could be too weakly constrained by those moments; or (iii) the moments analyses
174   could have introduced systematic biases due to a failure of the CLT. To eliminate the first
175   explanation, we computed the Fisher Information Matrix (FIM) defined by the moments-based
176   analyses[24]. Because the computed FIM has full rank, we conclude that the model should be
177   identifiable. If the second explanation were true (i.e., if the moments-analyses had produced
178   weakly constrained models), then changing the parameters to those selected by the FSP analysis
179   should have only a small effect on the moment-based likelihood. In such a case, the FSP
180   parameters would lie within large parameter confidence intervals identified by the moments-
181   based analyses. However, using the experimental *STL1* data, we computed that the FSP
182   parameter set was $10^{2,750}$ less likely to have been discovered using means, $10^{14,500}$ less likely to
183   have been discovered using means and variances, and 10^{664} less likely to have been discovered
184   using the extended moments analysis (Table S5). Thus, we conclude that failure of the moments-
185   based analyses to match the distributions in Figs. 2, S2, and S3 cannot be explained by
186   uncertainty alone.
187
188   To test the third explanation for parameter estimation failure (i.e., systematic bias), we used the
189   FSP parameters and generated simulated data for the mean (Fig. 3A), standard deviation (Fig.
190   3B), and the ON-fraction (Fig. 3C) versus time for *STL1* mRNA under an osmotic shock of 0.2M
191   NaCl. As shown in Fig. 3A,B, the *median* of the simulated data sets (magenta) matches the
192   experimental data (red and cyan) at all times, but at later times (>20 minutes) both are
193   consistently less than the theoretical values (black). This mismatch is due to finite sampling from
194   asymmetric distributions especially at later time points (Fig. 3D). The Gaussian assumption
195   applied to the first two moments analyses[24], which does not account for asymmetry, imposes
196   narrow and nearly symmetric likelihood functions for the sample mean and sample variance
197   (cyan lines in Fig. 3E,F, respectively). These moment-based likelihood functions are inconsistent
198   with the actual sample statistic distributions (Fig. 3F, compare cyan and black lines). Because the
199   mRNA distributions are very broad at late time points (Fig. 3D), one would need to measure 10^5
200   or 10^7 cells to estimate the variance within 10% or 1%, respectively (Fig. 3G). Furthermore,
201   because the mRNA distributions are highly asymmetric, measurements are likely to repeatedly
202   underestimate the summary statistics. As a result, the moment-based likelihood functions were
203   deleteriously overfit to underestimated mRNA expression at late time points, and resulted in
204   excessively confident overestimation of the mRNA degradation rate (Table S3). In principle, the

205   extended moments analysis could better capture the correct likelihood function for the sample
206   statistics (Figs. 3E,F magenta lines), but this requires *a prior* knowledge of the exact third and
207   fourth moments. In practice, because those higher order statistics must be estimated using the
208   model, the resulting extended moments analysis was less biased but more uncertain.
209
210   *Full distribution analyses substantially reduce model uncertainty and bias.* To confirm the
211   tradeoff between uncertainty and bias, we applied the Metropolis Hastings algorithm (MHA) to
212   analyze parameter variation for the different likelihood functions and to estimate parameter
213   uncertainty and bias (Fig. 4A-C)[24]. Comparing the parameter variations for the transcription
214   initiation rate, k_{i3}, and the mRNA degradation rate, γ, illustrates that extending the analysis from
215   the means to means and variances can affect the parameter identification bias much more than
216   the parameter uncertainty (Fig. 4A). Moreover, this effect is not always advantageous; inclusion
217   of variances in the analysis led to substantially increased parameter bias for *STL1* (compare red
218   and blues ellipses in Fig. 4A,C and see Fig. S9) and relatively little change for *CTT1* (Figs. S10
219   and S11). In contrast, analyses using the FSP consistently reduced both uncertainty and bias for
220   both *STL1* and *CTT1* analyses (Figs. 4A-C and S9-S11).
221
222   *Using spatial fluctuations improves model identification*. Having established that different
223   stochastic fluctuation analyses attain different levels of uncertainty and bias, we asked if more
224   information could be extracted from spatially-resolved data. Using a nuclear stain, we quantified
225   the numbers of *STL1* and *CTT1* mRNA in the nucleus and cytoplasm[24] (Fig. 1B). We then
226   extended the model and our analyses to consider the joint cytoplasmic and nuclear mRNA
227   distributions (Fig. S4 and S5). From these analyses, we observed that spatial data reduced
228   parameter bias for the models, despite the addition of new parameters and model complexity
229   (Fig. 4A-C and S9-11).
230
231   *Measuring and predicting transcription site dynamics.* We next explored how well the identified
232   models could be used to predict the elongation dynamics of nascent mRNA at individual *STL1* or
233   *CTT1* transcription sites (TS, Fig. 1B,C). We quantified the TS intensity for *CTT1*, and we used
234   an extended FSP model for *CTT1* regulation to estimate the Polymerase II elongation rate to be
235   63±13 nt/s[24], a value consistent with published rates of 14-61 nt/s[28,29]. We assumed an identical
236   rate for the *STL1* gene, and we used the FSP model for *STL1* gene regulation to predict the *STL1*
237   TS activity (Figs. 1D, 4D). The spatial (non-spatial) FSP model predicts an average of 7.0 (9.3)
238   full length *STL1* mRNA per active TS, a value that matches well to our measured value of 4.2-
239   7.5 *STL1* mRNA per active TS. However, predictions using parameters identified from
240   moments-based analyses were incorrect by several orders of magnitude (Fig. 1D). In addition to
241   predicting the average number of nascent mRNA per active TS, the FSP model also accurately
242   predicts the fraction of cells that have an active *STL1* TS versus time as well as the distribution
243   of nascent mRNA per TS (Figs. 4E).
244
245   **Discussion**
246
247   Integrating stochastic models and single-molecule and single-cell experiments can provide a
248   wealth of information about gene regulatory dynamics[14]. In previous work, we discussed the
249   importance to *choose the right model* to match the single-cell fluctuation information and
250   achieve predictive understanding[18]. Here we have shown how important it is to *choose the right*

251   *computational analysis* with which to analyze single-cell data. We showed how model
252   identification based solely upon average behaviors can lead to substantial parameter uncertainty
253   and bias, potentially resulting in poor predictive power (Figs. 1-4). We showed how single-
254   molecule experiments often yield discrete, asymmetric distributions that are demonstrably non-
255   Gaussian (Figs. 2D,E, 3, S2, and S3), and how model extensions to include hard-to-measure
256   variances and covariances may exacerbate biases (Fig. 4C) leading to greatly diminished
257   predictive power (Figs. 1D). By taking into account the full distribution shapes, one can correct
258   these deleterious effects and obtain parameter estimates and predictions that are improved by
259   many orders of magnitude, even when applied to the same model and same data (Figs. 1D, 2, 4).
260   We stress that this concern occurs even for models for which exact equations are known and
261   solvable for the statistical moment dynamics. For more complex and nonlinear models, where
262   approximate moment analyses are required, these effects are likely to be exacerbated further.
263   This issue is expected to be even more relevant in mammalian systems, which exhibit greater
264   bursting[1,2,21] and for which data collection may be limited to smaller sizes (e.g., by increased
265   image processing difficulties for complex cell shapes or by small numbers of cells, as available
266   from an organ, a tissue from a biopsy, or for a rare cell type population).
267
268   Because most single-cell modeling investigations to date have used only means or means and
269   variances from finite data sets to constrain models, it is not surprising that many biological
270   models fail to realize predictive capabilities. Conversely, our full consideration of the single-
271   molecule distributions enabled discovery of a comprehensive model that quantitatively captures
272   transcription regulation with biologically realistic rates and interpretation for transcription
273   initiation, transcription elongation, and mRNA export and nuclear and cytoplasmic mRNA
274   degradation (Fig. 1A). We argue that the solution is not to collect increasingly massive amounts
275   of data, but instead to develop computational tools that utilize the full, unbiased spatiotemporal
276   distributions of single-cell fluctuations. By addressing the limitations of current approaches and
277   relaxing requirements for normal distributions or large sample sizes, our approach should have
278   general implications to improve mechanistic model identification for any discipline that is
279   confronted with non-symmetric datasets and finite sample sizes.
280
281   **Methods and Materials**
282
283   **Yeast strain and growth condition.** *Saccharomyces cerevisiae BY4741 (MATa; his3Δ1;*
284   *leu2Δ0; met15Δ0; ura3Δ0)* was used for time-lapse microscopy and FISH experiments. Cells
285   are grown in complete synthetic media (CSM, Formedia, UK) to an optical density (OD) of 0.5.
286   Nuclear enrichment of YFP C-terminus tagged Hog1 was measured in single cells over time in
287   response to osmotic stress[30,31].
288
289   **Microscopy setup for time-lapse and single molecule RNA FISH imaging.** Cells were imaged
290   with a Nikon Ti Eclipse epifluorescent microscope equipped with perfect focus (Nikon), a 100x
291   VC DIC lens (Nikon), fluorescent filters for YFP, DAPI, TMR and CY5 (Semrock), an X-cite
292   120 fluorescent light source (Excelitas), and an Orca Flash 4v2 CMOS camera (Hamamatsu).
293   The microscope was controlled by Micro-Manager program[32].
294
295   **Image acquisition for time-lapse and single molecule RNA FISH imaging.** Constant focus
296   mode live cell time-lapse microscopy was performed by taking bright field images every 10 s

297 and YFP fluorescent images every minute. Single molecule RNA-FISH microscopy was
298 performed as z-stacks of 200nm between images from fixed yeast cells for bright field, DAPI,
299 TMR and CY5.

300

301 **Sample preparation for live cell time-lapse microscopy.** Hog1-YFP tagged yeast cells are
302 loaded into a flow chamber[33]. CSM or CSM with 0.2M or 0.4M NaCl was passed through the
303 flow chamber using a syringe pump (New Era Pump Systems) at a pump rate of 0.1 ml/minute.

304

305 **Image analysis for time-lapse microscopy.** The bright field and YFP images are background
306 corrected and smoothed. The YFP images are then thresholded and converted to a binary image
307 resulting in a nuclear marker for cell segmentation. The processed bright field and the binary
308 YFP images were combined using morphological reconstruction, and cells were segmented with
309 a watershed algorithm. After segmentation, the centroid of each cell was computed and tracked
310 over time to generate single cell time trajectories. For each cell the Hog1 nuclear enrichment
311 was then calculated as $Hog1(t) = [(I_t(t) - I_b) / (I_w(t) - I_b)]$, with I_w (average per pixel fluorescent
312 intensity of the whole cell), I_b (average per pixel fluorescent intensity of the camera background),
313 and I_t (average per pixel fluorescent intensity of the 100 brightest fluorescent pixels). The single
314 cell traces were smoothed and subtracted by the $Hog1(t)$ signal on the beginning of the
315 experiment. For cell volume measurements, volume change relative to the volume at the
316 beginning of the experiment was calculated. The median and the average median distance
317 (standard deviation of the median) from single cell time traces of Hog1- YFP and cell volume
318 was computed. The final time-lapse microscopy data set consist of 246 (0.2M NaCl) and 167
319 (0.4M NaCl) cells. Each time course was measured in duplicates or triplicates.

320

321 **Sample preparation for single-molecule RNA-FISH.** Yeast cells (OD = 0.5) was concentrated
322 tenfold through a filter system, then exposed to NaCl concentration of 0.2 M and 0.4 M NaCl,
323 and then fixed in 4 % formaldehyde at time points 0, 1, 2, 4, 6, 8, 10, 15, 20, 25, 30, 35, 40, 45,
324 50, 55 minutes after osmotic stress. After fixation, cells are spheroplasted with 2.5 mg/ml
325 Zymolyase (US Biological) until cells turn from an opaque to a black color. Cells are stored in
326 70 % ethanol at +4C for at least 12 hours. Hybridization and RNA-FISH probe preparation
327 conditions were applied as published[18]. Table S1 contains the RNA-FISH probes for *STL1* and
328 *CTT1*. Each time course was measured in duplicate or triplicate.

329

330 **Image analysis for single-molecule RNA-FISH.** Each DAPI image stack was maximum
331 intensity projected, thresholded, converted into a binary image, and individual connected regions
332 of biologically relevant size was segmented resulting in individually labeled nuclei. For each
333 cell, the entire DAPI image stack was converted into a binary image stack using cell specific
334 DAPI thresholds resulting in 3D thresholded nucleus and cytoplasm. The last 5 images of the
335 bright field image stack were maximum projected to generate the cell outlines. This image was
336 background corrected and combined with the threshold DAPI image using morphological
337 reconstruction and cells were segmented with a watershed algorithm. To identify RNA spots, a
338 fluorescent intensity threshold was determined for each dye, and each field of view imaged. For
339 a specific time course experiment, the average fluorescent threshold was determined from the
340 average of all the individual thresholds. After the thresholds had been determined each image in
341 the stack was Gaussian filtered, filtered with a Laplacian of a Gaussian filter to detect punctuate
342 in the image, converted into binary images using the previously determined threshold, and the

343 regional maxima was determined within the image stack. A mask of segmented nucleus and
344 cytoplasm was applied to the filtered RNA-FISH image stacks and the numbers of RNA spots
345 were counted in each compartment for each cell in three dimensions. To determine the number
346 of transcripts of each transcription site, we determined the total intensity of each RNA spot in the
347 cell. We also fitted each RNA spot with a 2D Gaussian function to determine the RNA spot
348 intensity and found very good agreement between the fitted and the total RNA spot intensities.
349 The total RNA-FISH data set consists of a total of 65454 single cells (25511 at 0.2M NaCl and
350 39943 at 0.4M NaCl).
351

352 **RNA-FISH data analysis.** For each time point, a distribution of mRNA molecules in single cells
353 was determined as the marginal distribution of total *STL1* and *CTT1* mRNA or as the joint
354 probability distribution of nuclear and cytoplasmic RNA. The distributions were also
355 summarized in a binary data set of ON-cells and OFF-cells. Cells with three or more mRNA
356 molecules were considered ON-cells for quantification of the ON-fraction. The population
357 average was computed as the mean marginal cytoplasmic or nuclear RNA for each mRNA
358 species. To quantify transcription site intensities, we recorded the intensity of all spots in the
359 nuclei for all cells. The brightest nuclear spots of each cell were labeled as potential
360 transcription sites, and were temporarily removed from the data set. We then computed the
361 median intensity for the remaining nuclear spots, and we used this median value to define the
362 equivalent mature nuclear mRNA fluorescence intensity. Next, we re-examined the brightest
363 RNA spot in each nucleus (i.e., the potential transcription sites), and we computed the
364 fluorescence intensity in units of mature mRNA intensities. Potential transcription sites that had
365 intensities greater than the equivalent of two mature mRNA molecules were labeled as active
366 transcription sites. This approach was applied to all cells from a single experiment. From this
367 analysis, we computed the fraction of cells with an active transcription site as a function of time,
368 the single-cell distributions of full length RNA transcripts per transcription site as a function of
369 time, and the average number of full length RNA transcripts per transcription site as a function
370 of time.
371

372 **Hog1-Kinase Model.** To model the temporally-varying Hog1p localization signal, we adopt the
373 model from[18], and we fit parameters of this model to the measured Hog1p nuclear enrichment
374 levels as functions of time, and osmolyte concentrations (see Table S2 and Fig. S1). This time-
375 varying signal has been used as an input to the gene regulation models.
376

377 **Gene Regulation Model.** To capture the spatial stochastic expression of *STL1* or *CTT1* mRNA,
378 the four-state *Hog1p*- activated gene expression model identified in Ref. 18 was extended to
379 account for spatial localization of mRNA in the nucleus or cytoplasm (see Fig. 1A). In total,
380 there are 13 non-spatial or 15 spatial parameters in the model.
381

382 **Computation of Moments**. Moment dynamics were analyzed using sets of coupled linear time-
383 varying ordinary differential equations. Theses ODEs provide exact expressions for the
384 dynamics of the model's means, variances, covariances and higher moments[34]. Because the
385 reaction rates are all linear, these moment equations are closed, and the moments can be
386 computed with no assumption on the distribution shape.
387

Computation of Full Distributions. Distributions were computed using the Finite State Projection approach[26] to approximate the exact solution of the Chemical Master Equation.

Computation of Moment-Based Likelihood Functions. To compare computed moments to measured experimental data required computation of the likelihood that the measured moments (e.g., means or covariance matrix) would have been observed by chance given that the model were correct. Three different approaches were derived to compute the likelihood of the observed moments given the model. First, to estimate the likelihood that the average data could come from the model, fluctuations were assumed to be Gaussian, with the model-generated means and the measured sample (co)variances. Second, to compute the likelihood to observe both the measured sample variance (non-spatial) or covariance matrix (spatial), the chi-squared distribution (non-spatial) or Wishart distribution (spatial) were used to approximate the likelihood to obtain the measured sample means and variances, given the model[35]. Third, the approach from Ref. 17 (based upon application of the central limit theorem) was used to approximate the joint likelihood to simultaneously measure the join sample means and sample covariance matrix in which the co-variance of the first two moments was assumed to depend upon the first four moments of the model at each condition and point in time.

Computation of the Full Distribution Likelihood. The likelihood of the full distribution data was computed using the FSP approach, similar to the approach taken in Refs. 18,36.

Parameter Searches to Maximize Likelihood. Iterative combinations of simplex based searches and genetic algorithm based searches were used to maximize likelihood functions. All parameters were defined to have positive values, and searches were conducted in logarithmic space. The searches are run multiple times from different starting parameter guesses leading to many tens of millions of function evaluations ($>4 \times 10^7$ evaluations of the means and moments analyses, $>5 \times 10^6$ evaluations of the non-spatial FSP distributions, and $>5 \times 10^5$ evaluations for the more computationally expensive analyses of extended moments and the spatial FSP distributions). Parallel fits were conducted on clusters of more than 128 processors at a time allowing for the consideration of several millions of model/parameter/experiment combinations per day.

Quantification of Parameter Uncertainties. The Metropolis Hastings algorithm[37] was used to quantify the parameter uncertainties. All MCMC parameter explorations were conducted in logarithmic parameter space, and all analyses (i.e., means, means and variances, or distributions, both spatial and non-spatial) used the same proposal distribution for the MCMC chains. This proposal distribution was a symmetric normal distribution (in logarithmic space) with a variance of 0.005 (also in logarithmic space). For each parameter proposal, a random selection of parameters was selected to change, where each parameter had a 50% chance to be perturbed. The first half of each chain was discarded as an MCMC burn-in period, and all chains were thinned by 90%. MCMC chains for the means and simpler moments analyses were run for MH chains with lengths of 1,000,000 parameter evaluations. MCMC analyses for the more computationally expensive extended moment analyses were run for at least 120,000 parameter evaluations. MCMC analyses for the non-spatial distribution analyses were run for at least 250,000 parameter evaluations. MCMC analyses for the most computationally expensive spatial distribution analyses were run for at least 15,000 parameter evaluations. To evaluate convergence of the

434 MCMC analyses, multiple MCMC chains were run for each analysis. To illustrate the achieved
435 convergence, Fig. S8 shows the similarity of distributions of likelihood values for two
436 independent MCMC runs for each analysis and for *STL1* and *CTT1*. The total bias and total
437 uncertainty, shown in Figs. 4B, 4C, S11B and S11C, were computed as described in the
438 supplemental material.
439

440 **Predictions of Transcription Site Activity.** Two different analyses were developed to predict
441 transcription site (TS) activity: a simplified theoretical analysis of average active TS activity and
442 an extended FSP analysis of distributions of polymerases on a given TS. In the *simplified*
443 *analysis*, it was assumed than an *active* TS would correspond to one gene at steady state with the
444 maximum transcription rate, $k_{i\text{-max}}$. Under this assumption, the average number of elongating
445 polymerases is given by $<n_{pol}> = k_{i\text{-max}}\tau_{elong} = k_{i\text{-max}}L/k_{elong}$. The average nascent mRNA was
446 assumed to be half the length of a mature mRNA, and since smFISH probes were equally
447 distributed along the length of the gene, the average nascent mRNA was assumed to exhibit half
448 the brightness of a mature mRNA. An *extended FSP approach* similar to that in (38) was also
449 used to compute the distribution for the number of polymerases at the TS. Under the assumption
450 that each partially transcribed mRNA was at a random location in the gene, its effective intensity
451 was approximated to be uniformly distributed between zero and the equivalent of one mature
452 mRNA. The distribution of TS spot intensities with N_{poly} polymerases was found through the
453 convolution of N_{poly} independent random variables, each with a uniform distribution between
454 zero and one. The FSP analysis was confirmed using an adapted form of the Stochastic
455 Simulation Algorithm[39] but with a modification[40] to allow for time varying reaction rates (Fig.
456 S12). For both experimental and computational analyses, TS sites were labeled as ON if their
457 predicted or measured intensities were greater than twice the intensity of a single mature mRNA.
458

459 **Identification of mRNA Elongation Rate.** The transcription elongation rate was found by
460 computing the TS intensity distribution for *CTT1* at each point in time for 0.2M and 0.4M NaCl
461 osmotic shock using the previously identified parameters (Table S4) and one free constant to
462 describe the average elongation rate, k_{elong}. The probability that the observed distributions of
463 *CTT1* TS intensities could have originated from this model was computed for all time points and
464 conditions, and as a function of k_{elong}. This likelihood was maximized for the different biological
465 replicas and NaCl concentrations to determine the uncertainty in this parameter. The simplified
466 theoretical model, which does not account for transitions between active and inactive periods,
467 provided an *upper bound* on the *CTT1* elongation rates to be 91±9Nt/s. The more detailed spatial
468 FSP approach determined the *CTT1* elongation rates to be 63±14Nt/s. For both cases, the
469 uncertainty is given as the standard error of the mean using the five experimental replicas (two
470 for 0.2M NaCl and three for 0.4M NaCl). The elongation rate was then fixed to be 63Nt/s, and
471 this rate was used in conjunction with the previously identified parameters to predict the TS
472 intensity distributions for *CTT1* and *STL1* as functions of time in both osmotic shock conditions
473 (Figs. 1D, 4D,E and S11D-H).
474

475 **Codes**. All computational results presented in this paper can reproduced using the provided
476 Matlab codes. The codes also include a simple GUI interface to generate additional figures: to
477 make predictions with changes to the identified parameters, to produce confidence ellipses for
478 new combinations of parameters, etc.
479

480

Acknowledgments

Contributions

BM and ZF designed and implemented the computational analyses. GL and GN designed and implemented the experimental analyses. BM, ZF, DS and GN wrote the manuscript.

Conflict of Interest

All authors have reviewed this manuscript, and there are no conflicts of interest.

References

1. Femino, A. M., Fay, F. S., Fogarty, K. & Singer, R. H. Visualization of Single RNA Transcripts in Situ. *Science* 280, 585–590 (1998).

2. Raj, A., van den Bogaard, P., Rifkin, S. A., van Oudenaarden, A. & Tyagi, S. Imaging individual mRNA molecules using multiple singly labeled probes. *Nature Methods* 5, 877–879 (2008).

3. Bendall, S. C. *et al.* Single-Cell Mass Cytometry of Differential Immune and Drug Responses Across a Human Hematopoietic Continuum. *Science* 332, 687–696 (2011).

4. Hammar, P. *et al.* Direct measurement of transcription factor dissociation excludes a simple operator occupancy model for gene regulation. *Nature genetics* 46, 405–408 (2014).

5. Gaublomme, J. T. *et al.* Single-Cell Genomics Unveils Critical Regulators of Th17 Cell Pathogenicity. *Cell* 163, 1400–1412 (2015).

6. Battich, N., Stoeger, T. & Pelkmans, L. Control of Transcript Variability in Single Mammalian Cells. *Cell* 163, 1596–1610 (2015).

7. Buenrostro, J. D. *et al.* Single-cell chromatin accessibility reveals principles of regulatory variation. *Nature* 523, 486–90 (2015).

8. Sepulveda, L. A., Xu, H., Zhang, J., Wang, M. & Golding, I. Measurement of gene regulation in individual cells reveals rapid switching between promoter states. *Science* 351, 1218–1222 (2016).

9. Morisaki, T. *et al.* Real-time quantification of single RNA translation dynamics in living cells. *Science* 352, 1425–1429 (2016).

10. Moffitt, J. R. *et al.* High-throughput single-cell gene-expression profiling with multiplexed error-robust fluorescence in situ hybridization. *Proceedings of the National Academy of Sciences* 113, 11046–11051 (2016).

11. Bintu, L. *et al.* Dynamics of epigenetic regulation at the single-cell level. *Science* 351, 720–724 (2016).

12. Frieda, K. L. *et al.* Synthetic recording and in situ readout of lineage information in single cells. *Nature* 541, 107–111 (2017).

13. Kumar, R. M. *et al.* Deconstructing transcriptional heterogeneity in pluripotent stem cells. *Nature* 516, 56–61 (2014).

14. Munsky, B., Neuert, G. & van Oudenaarden, A. Using Gene Expression Noise to Under-

525   stand Gene Regulation. *Science* 336, 183–187 (2012).

526 15. Zechner, C., Unger, M., Pelet, S., Peter, M. & Koeppl, H. Scalable inference of
527   heterogeneous reaction kinetics from pooled single-cell recordings. *Nature Methods* 11,
528   197–202 (2014).

529 16. Hilfinger, A., Norman, T. M. & Paulsson, J. Exploiting natural fluctuations to identify
530   kinetic mechanisms in sparsely characterized systems. *Cell systems* 2, 251–259 (2016).

531 17. Ruess, J., Milias-Argeitis, A. & Lygeros, J. Designing experiments to understand the
532   variability in biochemical reaction networks. *Journal of The Royal Society Interface* 10,
533   20130588–20130588 (2013).

534 18. Neuert, G. *et al.* Systematic Identification of Signal-Activated Stochastic Gene Regulation.
535   *Science* 339, 584–587 (2013).

536 19. Weinberger, L. S., Burnett, J. C., Toettcher, J. E., Arkin, A. P. & Schaffer, D. V. Stochastic
537   Gene Expression in a Lentiviral Positive-Feedback Loop: HIV-1 Tat Fluctuations Drive
538   Phenotypic Diversity. *Cell* 122, 169–182 (2005).

539 20. Suel, G. M. *et al.* Tunability and Noise Dependence in Differentiation Dynamics. *Science*
540   315, 1716–1719 (2007).

541 21. Raj, A., Rifkin, S. A., Andersen, E. & van Oudenaarden, A. Variability in gene expression
542   underlies incomplete penetrance. *Nature* 463, 913–918 (2010).

543 22. Balazsi, G., van Oudenaarden, A. & Collins, J. J. Cellular decision making and biological
544   noise: from microbes to mammals. *Cell* 144, 910–925 (2011).

545 23. Saito, H. & Posas, F. Response to Hyperosmotic Stress. *Genetics* 192, 289–318 (2012).

546 24. See Materials and Methods and supplemental information.

547 25. Peccoud, J. & Ycart, B. Markovian Modeling of Gene-Product Synthesis. *Theoretical*
548   *Population Biology* 48, 222–234 (1995).

549 26. Munsky, B. & Khammash, M. The Finite State Projection Algorithm for the Solution of the
550   Chemical Master Equation. *The Journal of Chemical Physics* 124, 044104 (2006).

551 27. Komorowski, M., Costa, M. J., Rand, D. A. & Stumpf, M. P. H. Sensitivity, robustness, and
552   identifiability in stochastic chemical kinetics models. *Proceedings of the National Academy*
553   *of Sciences* 108, 8645–8650 (2011).

554 28. Larson, D. R., Zenklusen, D., Wu, B., Chao, J. A. & Singer, R. H. Real-Time Observation
555   of Transcription Initiation and Elongation on an Endogenous Yeast Gene. *Science* 332, 475–
556   478 (2011).

557 29. Mason, P. B. & Struhl, K. Distinction and relationship between elongation rate and
558   processivity of RNA polymerase II in vivo. *Molecular Cell* 17, 831–840 (2005).

559 30. Muzzey, D., Gomez-Uribe, C. A., Mettetal, J. T. & van Oudenaarden, A. A Systems-Level
560   Analysis of Perfect Adaptation in Yeast Osmoregulation. *Cell*, 138(1), 160–171 (2009).

561 31. Ferrigno, P., Posas, F., Koepp, D., Saito, H. & Silver, P.A. Regulated nucleo/cytoplasmic
562   exchange of HOG1 MAPK requires the importin β homologs NMD5 and XPO1. *Embo J.*,
563   17(19), 5606–5614 (1998).

564 32. Edelstein, A. D., Tsuchida, M. A., Amodaj, N., Pinkard, H., Vale, R. D. & Stuurman, N.
565   Advanced methods of microscope control using µManager software. *Journal of Biological*
566   *Methods*, 1(2), e10 (2014).

567 33. Mettetal, J. T., Muzzey, D., Gomez-Uribe, C. & van Oudenaarden, A. The Frequency
568   Dependence of Osmo-Adaptation in Saccharomyces cerevisiae. *Science*, 319(5862), 482–
569   484 (2008).

570   34. Hespanha, J. P. & Singh, A. Stochastic models for chemically reacting systems using
571   polynomial stochastic hybrid systems. *International Journal of robust and nonlinear*
572   *control*, 15(15), 669–690 (2005).
573   35. Wishart, J. The Generalised Product Moment Distribution in Samples from a Normal
574   Multivariate Population. *Biometrika*, 20A(1/2), 32-52 (1928).
575   36. Fox, Z., Neuert, G. & Munsky, B. Finite state projection based bounds to compare chemical
576   master equation models using single-cell data. *J. Chemical Physics*, 145(7), 074101 (2016).
577   37. Chib, S. & Greenberg, E. Understanding the Metropolis-Hastings Algorithm. *The American*
578   *Statistician*, 49(4), 327–335 (1995).
579   38. Senecal, A., Munsky, B., Proux, F., Ly, N., Braye, F. E., Zimmer, C., Mueller, F. &
580   Darzacq, X. Transcription factors modulate c-Fos transcriptional bursts. *Cell Reports*, 8(1),
581   75–83 (2014).
582   39. Gillespie, D. T. Exact stochastic simulation of coupled chemical reactions. *J. Phys. Chem.*,
583   81, 2340–2361 (1977).
584   40. Voliotis, M., Thomas, P., Grima, R. & Bowsher, C. G. Stochastic Simulation of
585   Biomolecular Networks in Dynamic Environments. *PLoS Computational Biology*, 12(6),
586   e1004923 (2016).
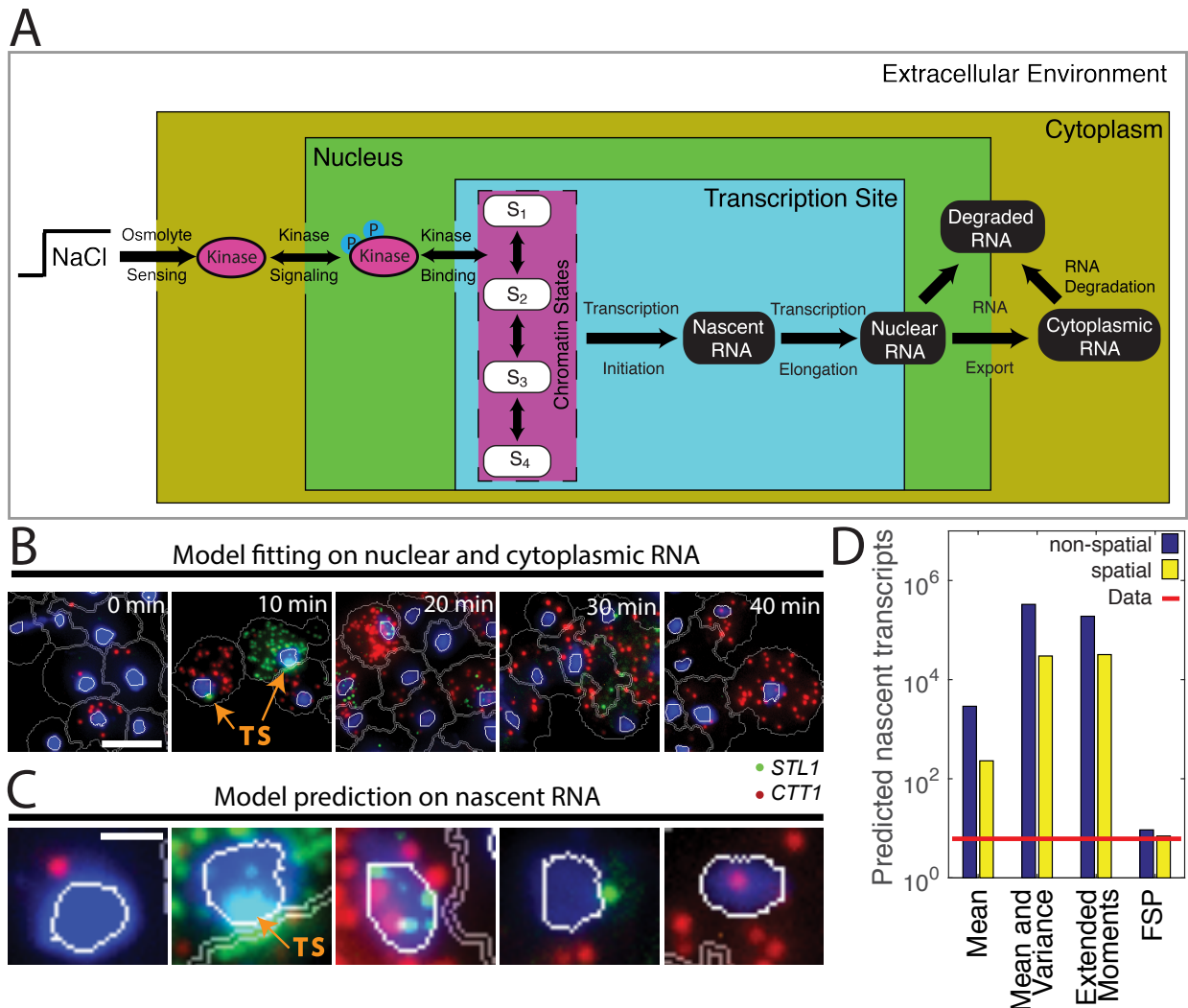
Figure 1. Discovering stochastic models to predict single-cell gene regulation. (A) Scope of the model to be identified, including quantitative analysis of MAPK induction and translocation, chromatin reorganization, polymerase initiation and elongation, and mRNA transcription, export, nuclear and cytoplasmic degradation. **(B)** Collection of single-cell spatiotemporal RNA transcription data to constrain the model (Fitting). Cytoplasmic and nuclear transcription quantification for expression of two mRNA species (*CTT1* in red and *STL1* in green). DAPI stained nucleus in blue. White line is the nuclear border, and the grey line is the cell boundary after automated segmentation. Representative images of cells exposed to 0.2M NaCl. 65454 cells in total have been imaged at 16 time points. Scale bar: 5μm. **(C)** Single-gene transcription site (TS) data used to validate the model (Prediction). Intensely bright spots within some cell nuclei are identified as transcription sites (TS). Scale bar: 1μm. **(D)** Validation of the model by comparing measured (solid red line) to predicted average number of nascent transcripts at active transcription sites using the same model and same data but under different modeling assumptions. Non-spatial analyses (blue) use the statistics (means, means and variances, or distributions) of the total number of RNA per cell. Spatial analyses (yellow) use the joint statistics of nuclear and cytoplasmic number of RNA per cell.
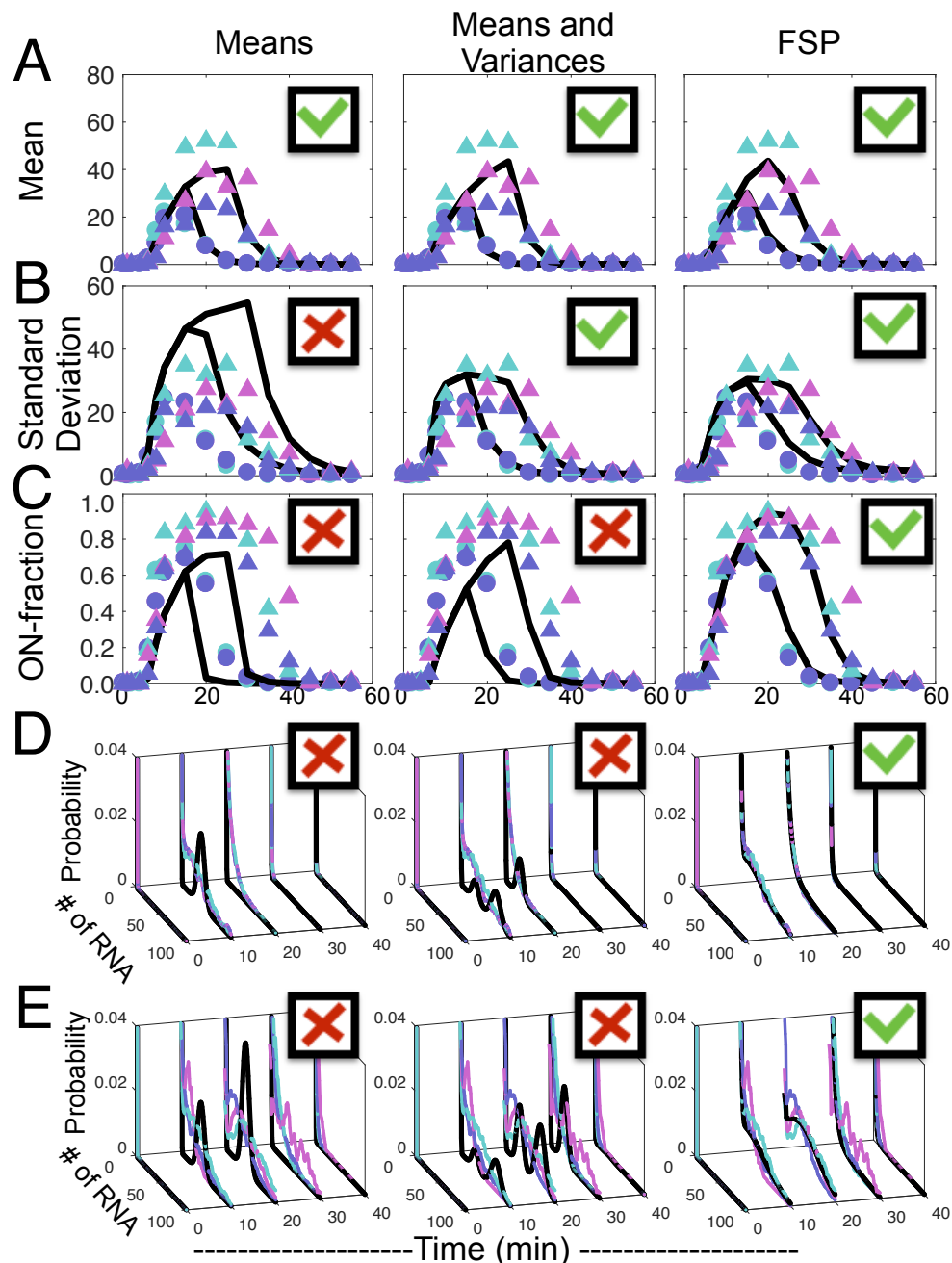
604
605 **Figure 2. Different computational analyses result in matches to different data statistics.** (**A**)
606 Mean number, (**B**) standard deviation, (**C**) ON-fraction (cells with >3 mRNA), and (**D,E**)
607 distributions of *STL1* mRNA copy number. In panels **A-C**, data for 0.2M NaCl (circles, two
608 biological replica) and 0.4M NaCl (triangles, three biological replica) are shown in magenta,
609 cyan, and violet, and model results are shown in black. Temporal distributions are measured at
610 (**D**) 0.2M NaCl and (**E**) 0.4M NaCl (cyan, violet, and magenta are biological replica). The left
611 column corresponds to the best fit to the measured mean; the center column corresponds to the
612 best fit to the measured means and variances; and the right column corresponds to the best fit to
613 the full measured distributions.
614
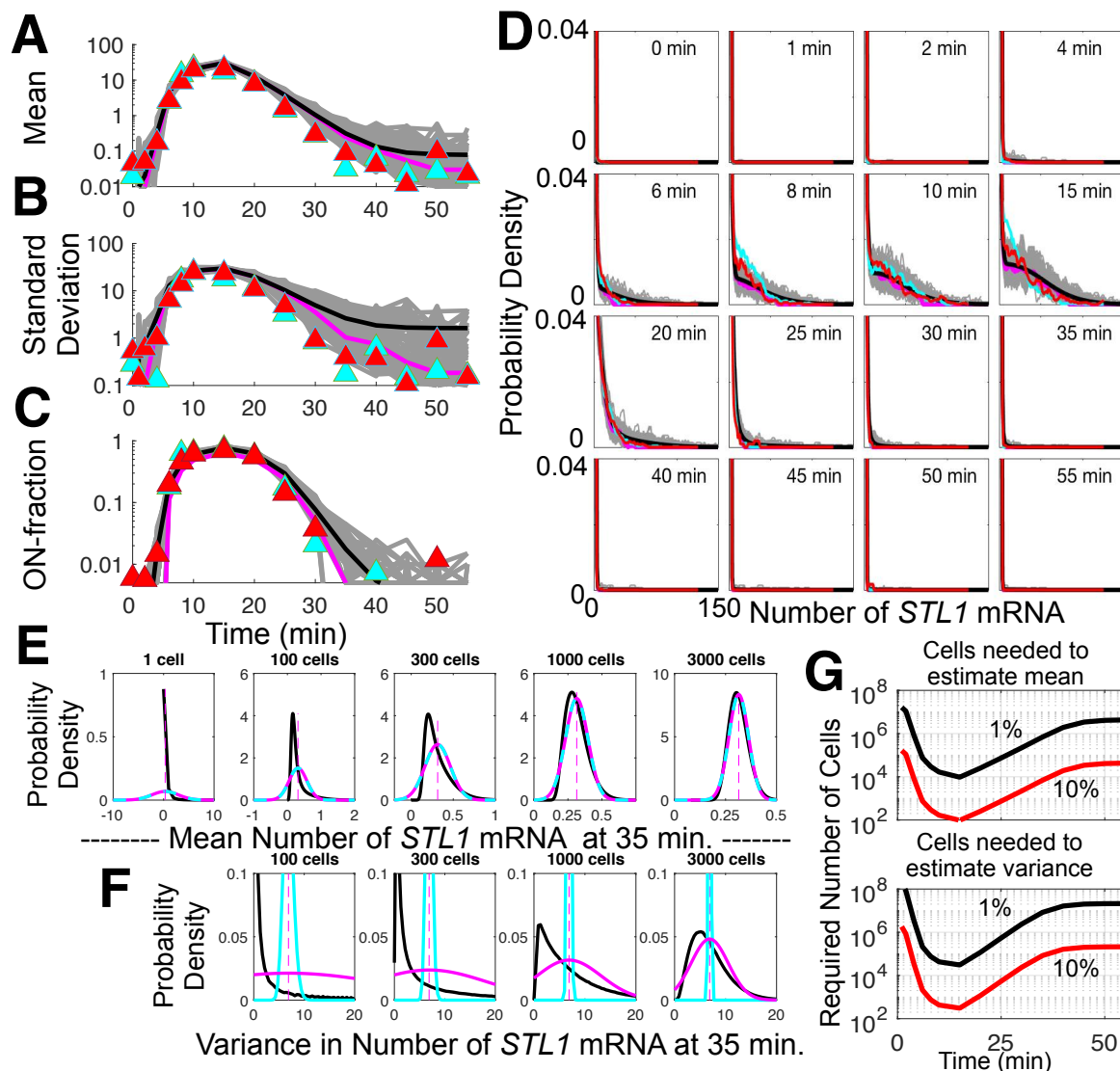
Figure 3. Discrete positive distributions introduce uncertainty and bias in parameter estimation. (**A**) Mean, (**B**) standard deviation, (**C**) ON-fraction, and (**D**) full distributions of *STL1* mRNA versus time for an osmotic shock of 0.2M NaCl applied at time $t = 0$. Theoretical values are in black, representative simulated samples of 200 cells each are in gray, median statistics of the simulated samples are in magenta; and experimental biological replica data are in red and cyan. (**E,F**) Expected distribution of sample mean (**E**) and sample variance (**F**) for *STL1* at 35 minutes computed using the CLT using Gaussian approximation (cyan), an extended moment analysis (magenta), or exact sampling from the FSP (black) for population sizes of 1, 100, 300, 1000, and 3000 cells. (**G**) Expected number of cells required to estimate the mean (top) or variance (bottom) within standard errors of 10% (red) or 1% (black). The dependence on time is due to the changing distribution shapes shown in Panel **D**.
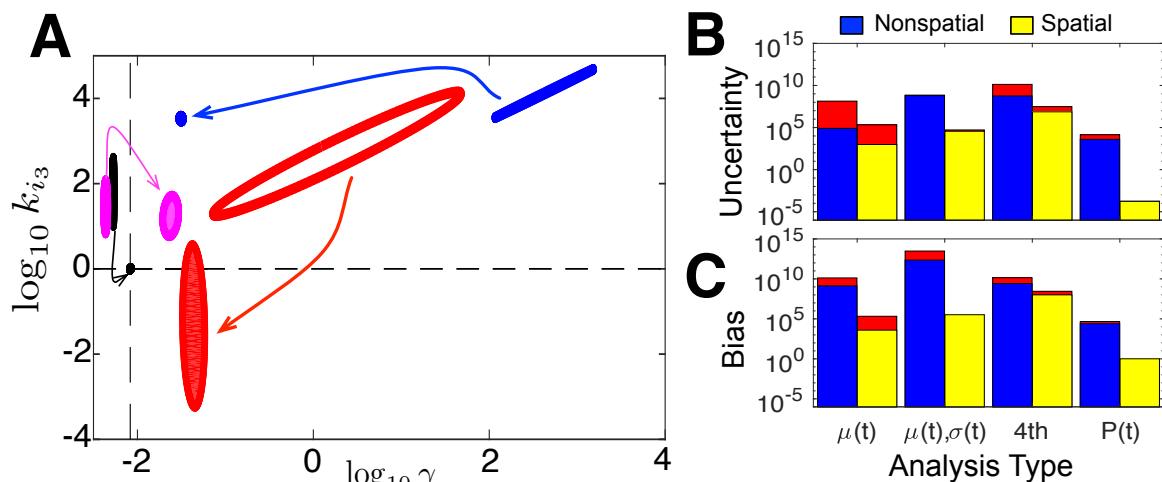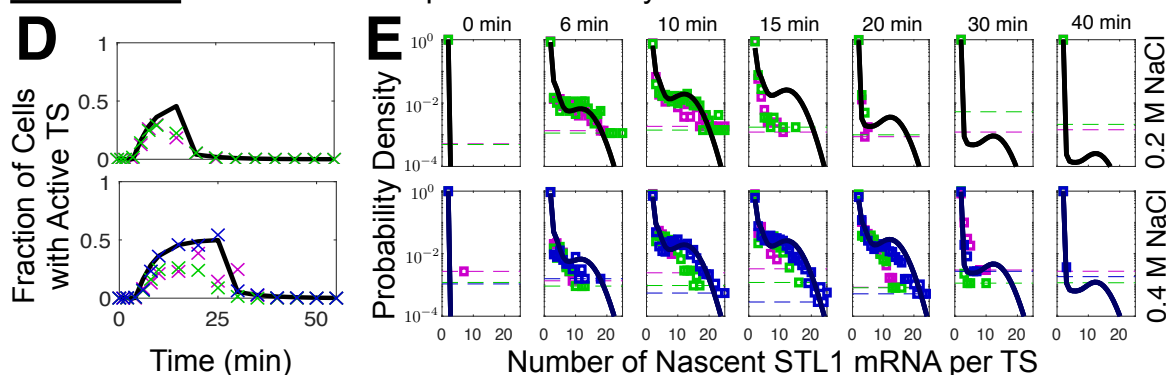
Figure 4. Stochastic and spatial fluctuation information improve parameter estimation to enable precise quantitative predictions. (**A**) Ninety percent confidence ellipses for the degradation rate (γ) and the maximal transcription initiation rate (k_{i3}) using the means only ($\mu(t)$, red), means and variances ($\mu(t),\Sigma(t)$ blue), extended moment analyses (4th, magenta), or the full FSP distributions (**P**(t), black). Arrows show the effect of adding spatial information to the analyses. The dashed black lines show the fit parameters for the spatial FSP *STL1* model. (**B**) Total parameter uncertainty and (**C**) bias for the four analyses using non-spatial (blue) and spatial (yellow) analyses. The red regions show the difference between independent MHA chains. (**D**) Predicted (black) and measured (magenta, green and blue crosses) fractions of cells with active *STL1* TS versus time at 0.2M (top) NaCl and 0.4M (bottom) NaCl osmotic shock. (**E**) Predicted (black) and measured (magenta, green and blue) distributions of nascent *STL1* mRNA per TS at different times following 0.2M (top) NaCl and 0.4M (bottom) NaCl osmotic shock. Magenta, green and blue horizontal lines correspond to the minimum detection limit ($1/N_c$, where N_c is the number of cells measured at that time for the corresponding biological replica). All predictions are made using parameters estimated previously from the mature, spatial mRNA distributions.

Supplementary Materials for

Distribution Shapes Govern the Discovery of Predictive Models for Gene Regulation

Brian E. Munsky, Guoliang Li, Zachary R. Fox, Douglas P. Shepherd, Gregor Neuert

correspondence to: munsky@colostate.edu and gregor.neuert@vanderbilt.edu

Contents

List of Figures

List of Tables

1 Materials and Methods – Experimental

1.1 Yeast strain and growth conditon

Saccharomyces cerevisiae BY4741 (MATa; his3Δ1; leu2Δ0; met15Δ0; ura3Δ0) was used for time-lapse microscopy and FISH experiments. Three days before the experiment, yeast cells from a stock of cells stored at -80°C were streaked out on a complete synthetic media plate (CSM, Formedia, UK). The day before the experiment, a single colony from the CSM plate was inoculated in 5 ml CSM medium (pre-culture). After 6-12h, the optical density (OD) of the pre-culture was measured and the cells were diluted into new CSM medium to reach an OD of 0.5 the next morning.To assay the nuclear enrichment of Hog1 in single cells over time in response to osmotic stress, a yellow-fluorescent protein (YFP) was tagged to the C-terminus of endogenous Hog1 in *BY4741* cells through homologous DNA recombination [1] [2].

1.2 Microscopy setup for time-lapse and single molecule RNA FISH imaging

Cells were imaged with a Nikon Ti Eclipse epifluorescnet microscope equipped with perfect focus (Nikon), a 100x VC DIC lens (Nikon), fluorescent filters for YFP, DAPI, TMR and CY5 (Semrock), an X-cite 120 fluorescent light source (Excelitas), and an Orca Flash 4v2 CMOS camera (Hamamatsu). The microscope was controled by Micro-Manager program [3].

1.3 Image aquisition for time-lapse and single molecule RNA FISH imaging

For live cell time-lapse microscopy the microscope was operated in constant focus mode. Bright field images were taken every 10 s with an exposure time of 10 ms and the YFP fluorescent images are taken every 1 minute with an exposure time of 20 ms. For single molecule RNA-FISH microscopy, z-stacks of images from fixed yeast cells for bright field, DAPI, TMR and CY5 were taken with each image in the z-stack separated by 200 nm. For each sample, muliple positions on the slide were imaged to ensure large numbers of cells.

1.4 Sample preparation for live cell time-lapse microscopy

1.5 ml of yeast cells with Hog1-YFP in log-phase growth (OD=0.5) were pelleted by centrifugation, resuspended in 20 μl CSM medium, and loaded into a flow chamber as described in [4]. The media passing through the flow chamber was removed through a syringe (New Era Pump Systems) connected to a pump (pump rate 0.1 ml/minute) at the exit of the flow chamber. On the input of the flow chamber, a two-way valve was connected to switch between a beaker with CSM media and a beaker with CSM medium with a fixed concentration of NaCl (0.2M or 0.4M).

1.5 Image analysis for time-lapse microscopy

Each image from the fluorescent tagged Hog1-kinase (Hog1-YFP) was used to generate a background image by running a disk smoothing filter over the image. The background image was subtracted from the orginial YFP image to enhance contrast. This image was then smoothed twice with a median filter. From this image the mean pixel intensity for pixels above 50 counts was computed. This value serves as a threshold to convert the YFP image into a binary image in which high intensity YFP signal that is enriched in the nucleus, is used as a nuclear marker. The bright field image was smoothed with a disk filter to generate a background image. The background image was subtracted from the orginial brightfield image to enhance contrast. The processed YFP image and the processed brightfield image were combined using morphological reconstruction, and cells were segmented with a watershed algorithm. Cells that are too small, too big, or too close to the image borders were removed. This process was repeated for

each image. After segmentation, the centroid of each cell was computed and stored. Next, the distance between each centroid for each of the two consecutive images was compared. The cells in the two images that have the smallest distance were considered the same cell at two different time points. This whole procedure was repeated for each image resulting in single cell trajectories. For each cell the average per pixel fluorescent intensity of the whole cell (Iw) and of the top 100 brightest fluorescent pixels (It) was recorded as a function of time. In addition, fluorescent signal per pixel of the camera background (Ib) was reported. The Hog1 nuclear enrichment was then calculated as Hog1(t) = [(It(t) - Ib) / (Iw(t) - Ib)]. The single cell traces were smoothed and subtracted by the Hog1(t) signal on the beginning of the experiment. Next, each single cell trace was inspected and cells exhibiting large fluctuations due to poor cell segmentation and cell tracking were removed. During the time points when no fluorescent images were taken, the fluorescent signal from the previous time point was used to segment the cell. Taking images every 10 s with an exposure time of 10 ms using bright field imaging did not result in photobleaching of the fluorescent signal and resulted in better tracking reliability because cells had not moved significantly since the previous image. For cell volume measurements, each time trace was removed of outlier points that resulted from segmentation uncertainties. Volume change relative to the volume at the beginning of the experiment was calculated to compare cells of different volumes. For both, the single-cell volume and Hog1(t) fluorescent traces, the median and the average median distance (standard deviation of the median) was computed to put less weight on sporadic outliers due to the image segmentation process. The final time-lapse microscopy data set consist of 246 (0.2M NaCl) and 167 (0.4M NaCl) cells. Each time course was measured in duplicates or triplicates.

1.6   Sample preparation for single-molecule RNA-FISH

Yeast cell culture (*BY4741* WT) in log-phase growth (OD = 0.5) was concentrated 10X (OD = 5) by a glass filter system with a 0.45 μm filter (Millipore). Cells were exposed to a final osmolyte concentration of 0.2 M and 0.4 M NaCl, and then fixed in 4 % formaldehyde at time points 0, 1, 2, 4, 6, 8, 10, 15, 20, 25, 30, 35, 40, 45, 50, 55 minutes. At each time point, cells (5 ml) in the corresponding beaker were poured into a 15 ml falcon tube containing formaldehyde, resulting in cell fixation. Cells were fixed at +20C for 30 minutes, then transferred to +4C and fixed overnight on a shaker. After fixation, cells are centrifuged at 500 xg for 5 minutes, and then the liquid phase was discarded. The cell pellet was resuspended in 5 ml ice-cold Buffer B (1.2 M sorbitol, 0.1 M potassium phosphate dibasic, pH 7.5) and centrifuged again. After discarding the liquid phase, yeast cells were resuspended in 1 ml Buffer B, and transferred to 1.5 ml centrifugation tubes. Cells were then centrifuged again at 500 xg for 5 minutes and the pellet was resuspended in 0.5 ml Spheroplasting Buffer (Buffer B, 0.2 % βmercaptoethanol, 10 mM Vanadyl-ribonucleoside complex). The OD of each sample was measured and the total cell number for each sample was equalized. 10 μl of 2.5 mg/ml Zymolyase (US Biological) was added to each sample on a +4C block. Cells were incubated on a rotor for 20-40 minutes at +30C until the cell wall was digested. The cells turn from an opaque to a black color if they are digested. Cells were monitored under the microscope every 10 minutes after addition of Zymolyase and when 90 % of the cells turned black, cells were transferred to the +4C block to stop Zymolyase activity. Cells were centrifuged for 5 minutes, then the cell pellet was resuspended with 1 ml ice-cold Buffer B and spun down for 5 minutes at 500 xg. After discarding liquid phase, the pellet was gently re-suspended with 1 ml of 70 % ethanol and kept at +4C for at least 12 hours or stored until needed at +4C. Hybridization and RNA-FISH probe preparation conditions were applied as published [5]. Table S1 contains the RNA-FISH probes for *STL1* and *CTT1*. Each time course was measured in duplicate or triplicate.

1.7 Image analysis for single-molecule RNA-FISH

To segment cells and to define the cells nuclear and cytoplasmic compartment the following steps were taken. For each DAPI image stack, a maximum intensity projection was generated. A DAPI intensity threshold was picked by eye to identify the maximum number of nuclei in the image. Based on this threshold, the image was then converted into a binary image. Connected regions (nuclei) that were too big or too small were removed. Connected regions in the image were then labeled by individual numbers resulting in individual numbered nuclei. Next, for each connected region three individual DAPI thresholds were computed as 40 (low threshold) and 50 (middle threshold) % of the difference between the maximum DAPI signal minus the background DAPI signal. Through this iterative and cell specific thresholding, cell-to-cell differences in nuclei DNA concentration and DAPI staining were taken into account. For the transcription site analysis, the low threshold was used. For the determination of the nuclear and cytoplasmic joint probability mRNA distribution, the middle threshold was used. For each cell, the entire DAPI image stack was converted into a binary image stack using the cell specific DAPI thresholds resulting in 3D thresholded nucleus and cytoplasm. After the nucleus had been segmented, the last 5 images of the bright field image stack were maximum projected to generate the cell outlines. A background image was generated by running a disk smoothing filter over this image. The background image was subtracted from the maximum projected image to enhance contrast. This image was then combined with the thresholded DAPI image using morphological reconstruction and cells were segmented with a watershed algorithm. Cells that were too small, too big, or too close to the image borders were removed.

To identify RNA spots, fluorescent thresholds for RNA-FISH images were determined for each dye based on a single image plane, for each position imaged and for each sample. For a given dye, the mean threshold value was calculated based on the thresholds identified from each image in the data sets. This threshold was very reproducible from image to image and from person to person. After the threshold had been determined for each dye, each image in the stack was Gaussian filtered to remove noise, and then filtered with a laplacian of a Gaussian filter to detect punctuate in the image. These filtered images were then converted into binary images using the previously determined threshold. For each pixilated signal, the regional maxima was determined, which identifies the xyz-position of the RNA spot within each 3D image stack. This processes was repeated for each of the TMR and CY5 image stacks. The number of RNA spots for each cell in the cytoplasm or the nucleus was determined by applying the mask of segmented nucleus and cytoplasm on the filtered RNA-FISH image stacks in 3D. The numbers of RNA molecules in the nucleus and cytoplasm were counted for each individual cell.

In order to determine the number of transcripts of each transcription site, we determined the total intensity of each RNA spot in the cell. We also fitted each RNA spot with a 2D Gaussian function to determine the RNA spot intensity and found very good agreement between the fitted and the total RNA spot intensities. The total RNA-FISH data set consists of a total of 65454 single cells (25511 at 0.2M NaCl and 39943 at 0.4M NaCl).

1.8 RNA-FISH data analysis

For each time point, a distribution of mRNA molecules in single cells was determined as the marginal distribution of total *STL1* and *CTT1* mRNA or as the joint probability distribution of nuclear and cytoplasmic RNA. The distributions were also summarized in a binary data set of ON and OFF cells. Cells with three or more mRNA molecules were considered ON-cells for quantification of the ON-fraction. The population average was computed as the mean marginal cytoplasmic or nuclear RNA for each mRNA species.

To quantify transcription site intensities, we recorded the intensity of all spots in the nuclei for all cells. The brightest nuclear spots of each cell were labeled as potential transcription sites, and were temporarily removed from the data set. We then computed the median intensity for the remaining nuclear spots, and we used this median value to define the equivalent mature nuclear mRNA fluorescence intensity. Next,

we re-examined the brightest RNA spot in each nuclei (i.e., the potential transcription sites), and we computed the fluorescence intensity in units of mature mRNA intensities. Potential transcription sites that had intensities greater than the equivalent of two mature mRNA molecules were labeled as active transcription sites. This approach was applied to all cells from a single experiment. From this analysis, we computed the fraction of cells with an active transcription site as a function of time, the single-cell distributions of full length RNA transcripts per transcription site as a function of time, and the average number of full length RNA transcripts per transcription site as a function of time.

2   Methods–Computational

All computational analyses have been performed using Mathworks MATLAB. All analysis codes are downloadable at XXX and required data sets are available at YYY[1]. Once the files have been downloaded, all results and Figures (2-4 and S1-S11) can be generated by (1) opening MATLAB and navigating to the main directory, and running the function MUNSKY_2017_MAIN.M. This function will open a simple interface that allows the user to generate all figure and to manipulate system parameters.

2.1   Parameterizing the Hog1p signal

To model the temporally-varying Hog1p localization signal, we adopt the empirical model from [5]. In this model, the level for Hog1p(t) enrichment is assumed to have the form:

$$Hog1p^\star(t) \equiv \left(\frac{Hog1p(t)}{1 + Hog1p(t)/M} \right)^\eta = A \left(\frac{(1 - \mathrm{e}^{-r_1 t})\,\mathrm{e}^{-r_2 t}}{1 + \frac{(1 - \mathrm{e}^{-r_1 t})\mathrm{e}^{-r_2 t}}{M}} \right)^\eta, \tag{1}$$

where A and M define the saturation height and midpoint and are the same for all salt levels. See the supplemental information of [5] for the derivation of this function.

   The parameters $\{r_1, \alpha, \eta, A, M\}$ have been fit to match the newly measured Hog1p nuclear enrichment levels as functions of time, and osmolyte concentrations. The parameters are given in Table S2, and the corresponding fits to the new experimental data are shown in Fig. S1. This time-varying signal has been used as an input to the gene regulation models below.

2.2   Gene regulation model

To capture the spatial stochastic expression of *STL1* or *CTT1* mRNA, we extend the four-state *Hog1p*-activated gene expression model identified in [5] to account for spatial localization of mRNA in the nucleus or cytoplasm (see Fig. 1A, 1B). The model consists of a single gene that can occupy one of four different transcriptional states (S_1, S_2, S_3, S_4) and two chemical species: nuclear mRNA (m_{nuc}), and cytoplasmic mRNA (m_{cyt}). The gene can transition between the four possible states ($S_j \rightarrow S_k$) with the rates, $\{k_{jk}\}$. The rate of the state transition $S_2 \rightarrow S_1$ depends on the level of Hog1p according to the simple saturated linear form,

$$k_{21} \equiv \max \left\{ 0, k_{21}^{(0)} - k_{21}^{(1)} \mathrm{Hog1p}\,(t - t_0) \right\}, \tag{2}$$

where t is the time following the addition of NaCl, and t_0 is a time delay required to capture the short period between transcription initiation and dispersion of mature mRNA[2]. All other state transition rates are constant in time. Each state S_j allows transcription of mRNA in the nucleus with rate, k_{i_j}. For the spatial model, nuclear mRNA are transported to the cytoplasm with rate, η_r. mRNA are assumed to

---

[1] A GITHUB download page will be created upon acceptance of this manuscript.
[2] The time offset parameter t_0 is only necessary for the non-spatial model and is identified as nearly zero for the spatial model.

degrade at the rate γ. For the spatial model, a second degradation rate γ_{nuc} is assumed for the nuclear region.

In total, there are 13 non-spatial or 15 spatial parameters in the model:

$$\boldsymbol{\Lambda} \equiv \left[k_{12}, k_{21}^{(0)}, k_{21}^{(1)}, k_{23}, k_{32}, k_{34}, k_{43}, k_{i_1}, k_{i_2}, k_{i_3}, k_{i_4}, \gamma, t_0, \eta_{\text{r}}, \gamma_{\text{nuc}} \right]. \tag{3}$$

For parameter uncertainty quantification, we assume an independent, log-uniform prior on all parameters, and all parameter searches are conducted in logarithmic space.

2.3 Computation of statistical moments of gene regulation fluctuations

In this section, we provide the sets of ordinary differential equations (ODE's) that describe the moments of the proposed model.

2.3.1 First and second moments

The analysis of the first two moments (i.e., the means, variances and covariances) are a special case of the general form for the higher order moments described below in Section 2.3.2. Let $\mathbf{x}(t)$ denote the state of the system at any given time:

$$\mathbf{x}(t) \equiv [S_1(t), S_2(t), S_3(t), S_4(t), m_{\text{nuc}}(t), m_{\text{cyt}}(t)]^T. \tag{4}$$

For this study, $\mathbf{x}$ is a vector of five (non-spatial) or six (spatial) discrete, non-negative integers. Chemical reactions are random events that take the system from one state to another: $\mathbf{x}_i \to \mathbf{x}_j$. Each μth reaction can be described by its stoichiometry vector, $\boldsymbol{s}_\mu$, which describes the state change that occurs for that reaction (i.e., $\boldsymbol{s}_\mu = \mathbf{x}_j - \mathbf{x}_i$ if the μth reaction goes from $\mathbf{x}_i$ to $\mathbf{x}_j$) and its propensity function $w_\mu(\mathbf{x}, t)dt$, which describes the probability that such a reaction would occur in the infinitesimally small time step, dt.

For the *non-spatial model*, there are six unique state transition stoichiometries, one transcription reaction, and one degradation reaction, for a total of eight unique stoichiometry vectors. These can be combined into the stoichiometry matrix:

$$\mathbf{S}_{\text{nonspatial}} \equiv \begin{bmatrix} -1 & 1 & 0 & 0 & 0 & 0 & 0 & 0 \\ 1 & -1 & -1 & 1 & 0 & 0 & 0 & 0 \\ 0 & 0 & 1 & -1 & -1 & 1 & 0 & 0 \\ 0 & 0 & 0 & 0 & 1 & -1 & 0 & 0 \\ 0 & 0 & 0 & 0 & 0 & 0 & 1 & -1 \end{bmatrix}, \tag{5}$$

in which each row corresponds to one of the state variables, and each column corresponds to a reaction. The corresponding propensity functions can also be written in matrix-vector form for the *nonspatial models* as:

$$\mathbf{w}_{\text{nonspatial}}(\mathbf{x}, t)dt = \begin{bmatrix} k_{12} & 0 & 0 & 0 & 0 \\ 0 & k_{21}^{(0)} + k_{21}^{(1)} Hog1p(t) & 0 & 0 & 0 \\ 0 & k_{23} & 0 & 0 & 0 \\ 0 & 0 & k_{32} & 0 & 0 \\ 0 & 0 & k_{34} & 0 & 0 \\ 0 & 0 & 0 & k_{43} & 0 \\ k_{i_1} & k_{i_2} & k_{i_3} & k_{i_4} & 0 \\ 0 & 0 & 0 & 0 & \gamma \end{bmatrix} \begin{bmatrix} S_1(t) \\ S_2(t) \\ S_3(t) \\ S_4(t) \\ m(t) \end{bmatrix} dt \tag{6}$$

$$= \mathbf{W}_1(t)\mathbf{x}(t)dt, \tag{7}$$

7

Similarly, the spatial model has an additional two reactions corresponding to transport from the nucleus to the cytoplasm and an extra degradation term for the nuclear mRNA. The stoichiometry matrix for the *spatial model* can be written:

$$
\mathbf{S}_{\text{spatial}} \equiv \begin{bmatrix}
-1 & 1 & 0 & 0 & 0 & 0 & 0 & 0 & 0 & 0 \\
1 & -1 & -1 & 1 & 0 & 0 & 0 & 0 & 0 & 0 \\
0 & 0 & 1 & -1 & -1 & 1 & 0 & 0 & 0 & 0 \\
0 & 0 & 0 & 0 & 1 & -1 & 0 & 0 & 0 & 0 \\
0 & 0 & 0 & 0 & 0 & 0 & 1 & -1 & -1 & 0 \\
0 & 0 & 0 & 0 & 0 & 0 & 0 & 0 & 1 & -1
\end{bmatrix},
\tag{8}
$$

and the corresponding propensity functions can also be written as:

$$
\mathbf{w}_{\text{spatial}}(\mathbf{x}, t)dt = \begin{bmatrix}
k_{12} & 0 & 0 & 0 & 0 & 0 \\
0 & k_{21}^{(0)} + k_{21}^{(1)} Hog1p(t) & 0 & 0 & 0 & 0 \\
0 & k_{23} & 0 & 0 & 0 & 0 \\
0 & 0 & k_{32} & 0 & 0 & 0 \\
0 & 0 & k_{34} & 0 & 0 & 0 \\
0 & 0 & 0 & k_{43} & 0 & 0 \\
k_{i_1} & k_{i_2} & k_{i_3} & k_{i_4} & 0 & 0 \\
0 & 0 & 0 & 0 & \gamma_{\text{nuc}} & 0 \\
0 & 0 & 0 & 0 & \eta_{\text{r}} & 0 \\
0 & 0 & 0 & 0 & 0 & \gamma
\end{bmatrix} \begin{bmatrix}
S_1(t) \\
S_2(t) \\
S_3(t) \\
S_4(t) \\
m_{\text{nuc}}(t) \\
m_{\text{cyt}}(t)
\end{bmatrix} dt
\tag{9}
$$

$$
= \mathbf{W}_1(t)\mathbf{x}(t)dt,
\tag{10}
$$

With these definitions, the time-varying means $\boldsymbol{\mu}(t) = \mathbb{E}\{\mathbf{x}(t)\}$ of all species and the corresponding covariance matrix $\boldsymbol{\Sigma}(t) = \mathbb{E}\{[\mathbf{x}(t) - \boldsymbol{\mu}(t)][\mathbf{x}(t) - \boldsymbol{\mu}(t)]^T\}$ can be computed by integrating the linear ordinary differential equations:

$$
\frac{d}{dt}\boldsymbol{\mu}(t) = \mathbf{S}\mathbf{W}_1(t)\boldsymbol{\mu}(t)
\tag{11}
$$

$$
\frac{d}{dt}\boldsymbol{\Sigma}(t) = \mathbf{S}\mathbf{W}_1(t)\boldsymbol{\Sigma}(t) + \boldsymbol{\Sigma}(t)\mathbf{W}_1(t)^T\mathbf{S}^T + \mathbf{S}\text{diag}(\mathbf{W}_1\boldsymbol{\mu}(t))\mathbf{S}^T.
\tag{12}
$$

This integration has been performed using Mathworks MATLAB.

2.3.2   Higher moments of gene regulation fluctuations

In order to compute the likelihood to observe the first two moments of gene regulation fluctuations, it is necessary to compute the third and fourth moments of the fluctuations as well. These higher moments can also be described by a set of linear ODEs as follows. Let $\mathbb{E}\{\mathbf{x}^{\boldsymbol{\beta}}\}$ denote a higher order uncentered moment of the random vector $\mathbf{x}$:

$$
\mathbb{E}\{\mathbf{x}^{\boldsymbol{\beta}}\} \equiv \mathbb{E}\{x_1^{\beta_1} \cdot x_2^{\beta_2} \cdots x_N^{\beta_N}\}.
\tag{13}
$$

With this definition the dynamics of $\mathbb{E}\{\mathbf{x}^{\boldsymbol{\beta}}\}$ can be shown to evolve according to the differential equation [6, 7]:

$$
\frac{d}{dt}\mathbb{E}\{\mathbf{x}^{\boldsymbol{\beta}}\} = \frac{d}{dt}\mathbb{E}\{x_1^{\beta_1} \cdot x_2^{\beta_2} \cdots x_N^{\beta_N}\} = \mathbb{E}\left\{\sum_{\mu}^{M} w_{\mu}(\mathbf{x}, t) \left(\prod_{i}^{N}(x_i + S_{i,\mu})^{\beta_i} - \prod_{i}^{N} x_i^{\beta_i}\right)\right\}.
\tag{14}
$$

In the special case where all propensity functions are first order, then Eqn. 14 represents a closed system of equations, which can be integrated to solve for the first four uncentered moments.

2.4 FSP computation of probability densities of gene regulation fluctuations

To compute the full time varying probability distributions, we use a slightly different notation. Let $\mathbf{y}(t) = [i, j, k]$ denote the state of the system where i is the index of the current gene state, S_i, j is the number of nuclear mRNA, and k is the number of cytoplasmic mRNA. Let $P(\mathbf{y}(t)|\boldsymbol{\Lambda}, \mathbf{P}_0)$ denote the probability of the state $\mathbf{y}$ at time t conditioned upon the model $\boldsymbol{\Lambda}$ and the initial probability distribution at $t = 0$, given by the vector $\mathbf{P}_0$. For the 4-state model examined in this study, the index i can take four different values, $i \in \{1, 2, 3, 4\}$, and m_{nuc} and m_{cyt} could be any non-negative integer value, $\{0, 1, 2, \ldots\}$. The chemical master equation [8] can be written:

$$\frac{d}{dt}P(\mathbf{y}, t) = -\sum_{\mu} w_{\mu}(\mathbf{y}, t)P(\mathbf{y}, t) + \sum_{\mu} w_{\mu}(\mathbf{y} - \mathbf{s}_{\mu}, t)P(\mathbf{y} - \mathbf{s}_{\mu}, t), \tag{15}$$

where the sum is over all possible reactions.

We enumerate all possible states in the set $\{\mathbf{y}_1, \mathbf{y}_2, \ldots\}$, and we define the corresponding probability density mass vector as: $\mathbf{P}(t) = [P_1(t), P_2(t) \ldots]^T$. Using the Finite State Projection analysis [9, 10], we truncate the full probability mass vector to a finite set where the number of mRNA in the nucleus and cytoplasm are each bounded by finite numbers, N_{nuc} and N_{cyt}. We utilize use a nested enumeration, given by $\mathbf{y}_{I(i,j,k)} = [i, j, k]$, where $I(i, j, k) = N_{\text{states}}(N_{\text{nuc}} + 1)k + N_{\text{states}}j + i$.

With this enumeration, the Chemical Master Equation can be written in vector form as: $\frac{d}{dt}\mathbf{P}(t) = \mathbf{Q}(t)\mathbf{P}(t)$. We solve this equation in MATLAB using the stiff ODE solver, ODE15S. For comparison of the model to the experimental mRNA distributions, it is necessary to convert the $\mathbf{P}(t)$ into a marginal distribution of nuclear and cytoplasmic mRNA numbers. This is relatively easy to do, since

$$\rho_{\text{nuc,cyt}}(t) \equiv P(mRNA_{\text{nuc}} = j, mRNA_{\text{cyt}} = k|t) = \sum_{i=1}^{N_{\text{states}}} P_{I(i,j,k)}(t). \tag{16}$$

The FSP approach and moments analyses were verified to match all moments up to fourth order, each within 0.002%.

Now with this definition, we can compare model predictions and experimental data as described below.

2.5 Computation of Likelihood Functions – Moments Analyses

For a population sample of N_S cells in which the mRNA has been measured as $\{x_1, x_2, \ldots x_{N_S}\}$, the measured sample mean (μ_S) and unbiased sample variance estimate (σ_S^2) are:

$$\mu_S(t) \equiv \frac{1}{N_S} \sum_{i=1}^{N_S} x_i(t) \tag{17}$$

$$\sigma_S^2(t) \equiv \frac{1}{N_S - 1} \sum_{i=1}^{N_S} (x_i(t) - \mu_S(t))^2. \tag{18}$$

2.5.1 Application of Central Limit Theory

The moment analyses discussed in this article (i.e., Eqns. 12 and 14) provide exact expressions for the dynamics of the model's means, variances, covariances and higher moments. Because the reaction rates are all linear, these moment equations are closed, and the moments can be computed with no assumption on the distribution shape. To compare these computed moments to measured experimental data requires computation of the likelihood that the measured moments (e.g., means or covariance matrix) would have been observed by chance given that the model were correct. The standard practice for such a computation

is either to assume Gaussian deviations or to apply the Central Limit Theorem (CLT) as follows. Let $\tilde{x}_i$ be a set of independent and identically distributed random variables with finite mean, μ, and finite variance, σ^2, and let $\tilde{y}$ be the average of N_S such random numbers.

According to the CLT, as N_S becomes very large, the distribution of $\tilde{y}_{N_S}$ will approach a normal distribution with a mean of μ and a variance of σ^2/N_S. The CLT allows us to estimate the likelihood of the observed moments as discussed in the following sections. We note that if $\tilde{x}_i$ is normally distributed, then $\tilde{y}_{N_S}$ would be normally distributed for any number of cells. However, in the case where $\tilde{x}_i$ is very far from normally distributed (e.g., when its distribution has a very long asymmetric tail) then a larger number of cells will be required before the CLT becomes valid. Such is the situation observed for the later time points in Fig. 3, which result in poor estimation of the moments-based likelihood function.

2.5.2 Likelihood to observe measured means

2.5.2.1. Univariate Case – Non-Spatial Model

Assuming a finite variance, $\sigma^2(t)$, and a large numbers of cells, N_S, the CLT states that the sample mean of a population of cells will have a distribution that can be approximated by a normal distribution with mean μ_m and variance $\sigma^2(t)/N_S$:

$$P(\mu_S|\mathcal{M}) = \sqrt{\frac{N_S}{2\pi\sigma^2}} \exp\left(\frac{-(\mu_S - \mu_\mathcal{M})^2}{2\sigma^2/N_S}\right), \tag{19}$$

where $\mathcal{M}$ denotes the model under consideration. Taking the logarithm of this likelihood function yields:

$$\log P(\mu_S|\mathcal{M}) = \frac{1}{2}\left(\log N_S - \log(2\pi) - \log(\sigma^2)\right) - \frac{(\mu_S - \mu_\mathcal{M})^2}{2\sigma^2/N_S}. \tag{20}$$

We can now compute the log likelihood of the averaged data given our model (up to a constant, C_1), provided that: (1) we can compute the mean, and (2) the variance is known:

$$\log P(\mu_S|\mathcal{M}) = C_1 - \frac{1}{2}\log(\sigma^2) - \frac{(\mu_S - \mu_\mathcal{M})^2}{2\sigma^2/N_S}. \tag{21}$$

In the case where we are only using the average measurements to constrain the model, we replace the variance with the sample variance estimate:

$$\log P_{[\mu\ \text{only}]}(\mu_S|\mathcal{M}) \approx C_1 - \frac{1}{2}\log(\sigma_S^2) - \frac{(\mu_S - \mu_\mathcal{M})^2}{2\sigma_S^2/N_S} \tag{22}$$

$$= \hat{C}_1 - \frac{(\mu_S - \mu_\mathcal{M})^2}{2\sigma_S^2/N_S}. \tag{23}$$

In this expression, all terms that do not depend upon the model mean, $\mu_\mathcal{M}$, have been lumped into the constant $\hat{C}_1$.

2.5.2.2. Multivariate Case – Spatial Model

The spatial model has $n = 2$ observables: nuclear and cytoplasmic mRNA levels, but the analysis is quite similar. When the number of cells in each sample, N_S, is large, the distribution of the sample mean vector, $\boldsymbol{\mu}_S$, given the model can be approximated by a multivariate normal distribution with mean, $\boldsymbol{\mu}_\mathcal{M}$, and covariance $(1/N_S)\boldsymbol{\Sigma}$. The likelihood of observing the measured mean at a given time point can be written

$$P(\boldsymbol{\mu}_S|\mathcal{M}) = \sqrt{\frac{N_S^n}{(2\pi)^n|\boldsymbol{\Sigma}|}} \exp\left(\frac{-N_S}{2}(\boldsymbol{\mu}_S - \boldsymbol{\mu}_\mathcal{M})^T \boldsymbol{\Sigma}^{-1}(\boldsymbol{\mu}_S - \boldsymbol{\mu}_\mathcal{M})\right), \tag{24}$$

where the notation $|\boldsymbol{\Sigma}|$ denotes the determinant of the covariance matrix, $\boldsymbol{\Sigma}$. Taking the logarithm of this likelihood and collecting terms that do not depend on $\boldsymbol{\mu}_{\mathcal{M}}$ or $\boldsymbol{\Sigma}$ into a constant yields:

$$\log P(\boldsymbol{\mu}_S | \mathcal{M}) = C_2 - \frac{1}{2} \log |\boldsymbol{\Sigma}| - \frac{N_S}{2} (\boldsymbol{\mu}_S - \boldsymbol{\mu}_{\mathcal{M}})^T \boldsymbol{\Sigma}^{-1} (\boldsymbol{\mu}_S - \boldsymbol{\mu}_{\mathcal{M}}). \tag{25}$$

To attempt to identify the model without computation of the second moments, we must approximate $\boldsymbol{\Sigma}$ with the measured sample covariance estimate:

$$\boldsymbol{\Sigma} \approx \boldsymbol{\Sigma}_S = \frac{1}{N_S - 1} \sum_{i=1}^{N_S} (\mathbf{x}_i - \boldsymbol{\mu}_S)(\mathbf{x}_i - \boldsymbol{\mu}_S)^T. \tag{26}$$

For this special case, the likelihood reduces to:

$$\log P_{[\boldsymbol{\mu} \text{ only}]}(\boldsymbol{\mu}_S | \mathcal{M}) \approx C_2 - \frac{1}{2} \log |\boldsymbol{\Sigma}_S| - \frac{N_S}{2} (\boldsymbol{\mu}_S - \boldsymbol{\mu}_{\mathcal{M}})^T \boldsymbol{\Sigma}_S^{-1} (\boldsymbol{\mu}_S - \boldsymbol{\mu}_{\mathcal{M}}). \tag{27}$$

$$= \hat{C}_2 - \frac{N_S}{2} (\boldsymbol{\mu}_S - \boldsymbol{\mu}_{\mathcal{M}})^T \boldsymbol{\Sigma}_S^{-1} (\boldsymbol{\mu}_S - \boldsymbol{\mu}_{\mathcal{M}}). \tag{28}$$

As in the previous case, all terms that do not depend upon the model mean, $\boldsymbol{\mu}_{\mathcal{M}}$, have been lumped into the constant $\hat{C}_2$.

2.5.3 Likelihood to observe measured (co)variances

To estimate model parameters using the gene expression variance, it is necessary to compute the likelihood that we would observe the measured *sample variance* given the model. For a single observable variable (e.g., non-spatial model for a single mRNA species), the sample variance, σ_S^2, will be a random variable that depends upon the distribution of the number of mRNA per cell at the corresponding time-point.

In this work, we consider two different CLT-based approaches to approximate the likelihood to observe the measured sample variances. The first method assumes that the likelihood of the observed sample variance can be well approximated by a χ-squared distributed random variable, which is independent of the sample mean. This approximation would be exact if the underlying distribution had a Gaussian distribution. This approximation of the likelihood depends only upon the model's computation of the first two moments. The second method approximates the sample mean and sample (co)variances as multivariate Gaussian random variables [7], whose covariance depends upon the first four moments of the analysis (thus the need for the extended moments analysis described in Section 2.3.2). These analyses are described in greater detail as follows:

2.5.3.1. Univariate Case – χ^2 distribution approximation.

Using the assumption that the sample population is sufficiently large that $\sum_{i=1}^{N_S} x_i$ has a normal distribution, one could approximate the probability of observing the measured sample variance using the χ-squared distribution with $\kappa = N_S - 1$ degrees of freedom:

$$P(\xi) = \frac{1}{2^{\kappa/2} \Gamma\left(\frac{\kappa}{2}\right)} \xi^{\frac{\kappa}{2}-1} e^{-\frac{\xi}{2}}, \tag{29}$$

where $\xi = (N_S - 1)\sigma_S^2 / \sigma_{\mathcal{M}}^2$, and $\kappa = N_S - 1$. Or by change of variables, this can be written:

$$P\left(\sigma_S^2 | \mathcal{M}\right) = \frac{(N_S - 1)}{\sigma_{\mathcal{M}}^2} \frac{1}{2^{(N_S-1)/2} \Gamma\left(\frac{(N_S-1)}{2}\right)} \left(\frac{(N_S-1)\sigma_S^2}{\sigma_{\mathcal{M}}^2}\right)^{\frac{(N_S-1)}{2}-1} e^{-\left(\frac{(N_S-1)\sigma_S^2}{2\sigma_{\mathcal{M}}^2}\right)} \tag{30}$$

$$= \frac{1}{2^{(N_S-1)/2} \sigma_S^2 \Gamma\left(\frac{(N_S-1)}{2}\right)} \left(\frac{(N_S-1)\sigma_S^2}{\sigma_{\mathcal{M}}^2}\right)^{\frac{(N_S-1)}{2}} e^{-\left(\frac{(N_S-1)\sigma_S^2}{2\sigma_{\mathcal{M}}^2}\right)} \tag{31}$$

11

The logarithm of the likelihood of the observed sample variance (σ_S^2) given the model variance ($\sigma_{\mathcal{M}}^2$) is:

$$\log P_{[\mu \text{ and } \sigma^2]}\left(\sigma_S^2|\mathcal{M}\right) = C_3 - \frac{N_S - 1}{2}\log(\sigma_{\mathcal{M}}^2) - \frac{(N_S - 1)\sigma_S^2}{2\sigma_{\mathcal{M}}^2}, \tag{32}$$

where C_3 is the collection of all terms that do not depend upon μ or $\sigma_{\mathcal{M}}^2$.

2.5.3.2. Multivariate Case – Wishart distribution approximation.

To estimate the likelihood function for the observed variance and covariances in the multivariate case, we use a generalization of the χ-squared distribution (Eqn. 31), known as the Wishart distribution [11]. To define this likelihood function, let $\boldsymbol{\Sigma}_{\mathcal{M}}$ represent the covariance matrix generated by the model. Let $\mathbf{X}_S$ represent an N_S by n *centered* matrix of the measured data for N_S different independent measurements of n distinct chemical species:

$$\mathbf{X}_S = \begin{bmatrix} x_{1,1} - \mu_1 & x_{1,2} - \mu_2 & \dots & x_{1,n} - \mu_n \\ x_{2,1} - \mu_1 & x_{2,2} - \mu_2 & \dots & \vdots \\ \vdots & \vdots & \ddots & \vdots \\ x_{N_S,1} - \mu_1 & x_{2,2} - \mu_2 & \dots & x_{N_S,n} - \mu_n \end{bmatrix} \tag{33}$$

Define $\mathbf{S}_S$ as the $n \times n$ *scatter matrix* of the data, $\mathbf{S}_S = \mathbf{X}_S^T \mathbf{X}_S$. With these definitions, the Wishart distribution over the range of possible $\mathbf{S}$ can be written:

$$P\left(\mathbf{S}_S|\mathcal{M}\right) = \frac{1}{2^{\kappa n/2}\boldsymbol{\Gamma}_n\left(\frac{\kappa}{2}\right)}\frac{|\mathbf{S}_S|^{\frac{\kappa-n-1}{2}}}{|\boldsymbol{\Sigma}_{\mathcal{M}}|^{\frac{\kappa}{2}}}\exp\left(-\frac{\text{trace}\left(\boldsymbol{\Sigma}_{\mathcal{M}}^{-1}\mathbf{S}_S\right)}{2}\right), \tag{34}$$

where $\kappa = N_S - 1$ is the degrees of freedom.

Taking the logarithm of Eqn. 34 and collecting all terms that are independent of $\boldsymbol{\Sigma}_{\mathcal{M}}$ yields:

$$\log P_{[\boldsymbol{\mu} \text{ and } \boldsymbol{\Sigma}]}\left(\mathbf{S}_S|\mathcal{M}\right) = C_4 - \frac{\kappa}{2}\log|\boldsymbol{\Sigma}_{\mathcal{M}}| - \frac{\text{trace}\left(\boldsymbol{\Sigma}_{\mathcal{M}}^{-1}\mathbf{S}_S\right)}{2}. \tag{35}$$

Using the relationship $\boldsymbol{\Sigma}_S = (N_S - 1)^{-1}\mathbf{S}_S$, this reduces to a form analagous to that for the univariate case in Equation 32:

$$\log P_{[\boldsymbol{\mu} \text{ and } \boldsymbol{\Sigma}]}\left(\boldsymbol{\Sigma}_S|\mathcal{M}\right) = C_4 - \frac{N_S - 1}{2}\log|\boldsymbol{\Sigma}_{\mathcal{M}}| - \frac{(N_S - 1)\text{trace}\left(\boldsymbol{\Sigma}_{\mathcal{M}}^{-1}\boldsymbol{\Sigma}_S\right)}{2}. \tag{36}$$

2.5.3.3. Likelihood to observe measured means and (co)variances using the χ-squared/ Wishart approximation.

Assuming a (multivariate) normal distribution for the number of nuclear and cytoplasmic mRNA, the sample means and the sample variances (covariance matrix) would be statistically independent. Therefore, the log-likelihood to match both statistics for the univariate case is the sum of Eqns. 21 and 32 over all time points $k = \{1, 2, \dots, K\}$:

$$\log P_{[\mu \text{ and } \sigma^2]}\left(\mu_S, \sigma_S^2|\mathcal{M}\right) = C - \sum_{k=1}^{K}\left(\frac{N_k - 2}{2}\log\sigma_{\mathcal{M}}^2(t_k) + \frac{N_k}{2}\frac{\left(\mu_S(t_k) - \mu_{\mathcal{M}}(t_k)\right)^2}{\sigma_{\mathcal{M}}^2(t_k)}\dots\right.$$
$$\left.+\frac{(N_k - 1)\sigma_S^2(t_k)/\sigma_{\mathcal{M}}^2(t_k)}{2}\right). \tag{37}$$

12

Similarly, in the multivariate case, the log-likelihood to match both the measured sample mean vector, $\boldsymbol{\mu}_S$, and the measured sample covariance matrix, $\boldsymbol{\Sigma}_S$, can be found from the sum of Eqns. 28 and 36:

$$\log P_{[\boldsymbol{\mu} \text{ and } \boldsymbol{\Sigma}]} (\boldsymbol{\mu}_S, \boldsymbol{\Sigma}_S | \mathcal{M}) = C - \sum_{k=1}^{K} \left(\frac{N_k - 2}{2} \log |\boldsymbol{\Sigma}_{\mathcal{M}}| + \frac{N_k}{2} (\boldsymbol{\mu}_S - \boldsymbol{\mu}_{\mathcal{M}})^T \boldsymbol{\Sigma}_{\mathcal{M}}^{-1} (\boldsymbol{\mu}_S - \boldsymbol{\mu}_{\mathcal{M}}) \ldots \right.$$
$$\left. + \frac{(N_k - 1)\text{trace} \left(\boldsymbol{\Sigma}_S \boldsymbol{\Sigma}_{\mathcal{M}}^{-1} \right)}{2} \right). \quad (38)$$

Naturally, Eqn. 38 reduces to Eqn. 37 in the case of a single chemical species.

2.5.3.4. Likelihood to observe measured means and (co)variances using a multivariate Gaussian approximation.

For strongly skewed distributions (e.g., those measured in this study), the sample mean and sample variance both depend strongly upon the experimental sampling of the distribution tails. As a result, these statistics are not statistically independent. To account for this interdependence, the CLT may be used to approximate the joint likelihood of the sample means and sample (co)variances as a multivariate normally-distributed random vector. For two measured species (e.g., nuclear and cytoplasmic mRNA), this vector has five elements ($\mathbf{z} \equiv [\mu_1, \mu_2, \sigma_{11}, \sigma_{12}, \sigma_{22}]$), and its probability distribution can be written in the form [7]:

$$P(\mathbf{z}_S | \mathcal{M}) = (2\pi)^{-5/2} |\mathbf{Q}_{\mathcal{M}}|^{-1/2} \exp\left(-\frac{1}{2} (\mathbf{z}_S - \mathbf{z}_{\mathcal{M}})^T \mathbf{Q}_{\mathcal{M}}^{-1} (\mathbf{z}_S - \mathbf{z}_{\mathcal{M}}) \right) \quad (39)$$

where $\mathbf{z}_S$ is the vector of measured means, variances and covariances; $\mathbf{z}_{\mathcal{M}}$ is the corresponding model-predicted average of those statistics; and $\mathbf{Q}_{\mathcal{M}}$ is the model-predicted covariance matrix for those statistics. The matrix $\mathbf{Q}_{\mathcal{M}}$ can be defined in terms of the second through fourth order moments as follows [7]:

$$\mathbf{Q}_{\mathcal{M}} \equiv \frac{1}{N_S} \begin{bmatrix} \sigma_{11} & \sigma_{12} & \sigma_{111} & \sigma_{112} & \sigma_{122} \\ \sigma_{12} & \sigma_{22} & \sigma_{112} & \sigma_{122} & \sigma_{222} \\ \sigma_{111} & \sigma_{112} & \sigma_{1111} - \frac{N_S-3}{N_S-1}\sigma_{11}^2 & \sigma_{1112} - \frac{N_S-3}{N_S-1}\sigma_{11}\sigma_{12} & \sigma_{1122} - \frac{N_S-3}{N_S-1}\sigma_{11}\sigma_{22} \\ \sigma_{112} & \sigma_{122} & \sigma_{1112} - \frac{N_S-3}{N_S-1}\sigma_{11}\sigma_{12} & \sigma_{1122} - \frac{N_S-2}{N_S-1}\sigma_{12}^2 + \frac{1}{N_S-1}\sigma_{11}\sigma_{22} & \sigma_{1222} - \frac{N_S-3}{N_S-1}\sigma_{12}\sigma_{22} \\ \sigma_{122} & \sigma_{222} & \sigma_{1122} - \frac{N_S-3}{N_S-1}\sigma_{11}\sigma_{22} & \sigma_{1222} - \frac{N_S-3}{N_S-1}\sigma_{12}\sigma_{22} & \sigma_{2222} - \frac{N_S-3}{N_S-1}\sigma_{22}^2 \end{bmatrix}_{\mathcal{M}}, \quad (40)$$

where $\sigma_{\beta_1 \ldots \beta_N}$ is used to denote the $(\sum \beta_i)^{\text{th}}$ centered moment:

$$\sigma_{\beta_1 \ldots \beta_N} \equiv \mathbb{E} \left\{ \prod_{i=1}^{N} (x_i - \mathbb{E}\{x_i\})^{\beta_i} \right\}. \quad (41)$$

Under this approximation, the logarithm of the the likelihood can be written:

$$\log(P(\mathbf{z}_S | \mathcal{M})) = C - \frac{1}{2} \log |\mathbf{Q}_{\mathcal{M}}| - \frac{1}{2} (\mathbf{z}_S - \mathbf{z}_{\mathcal{M}})^T \mathbf{Q}_{\mathcal{M}}^{-1} (\mathbf{z}_S - \mathbf{z}_{\mathcal{M}}), \quad (42)$$

and the log-likelihood for all time points, $k = 1, \ldots, K$ can be written:

$$\log P_{\text{MV-Gaussian}} (\{\mathbf{z}(t_k)\} | \mathcal{M}) = C - \frac{1}{2} \sum_{k=1}^{K} \left(\log |\mathbf{Q}_{\mathcal{M}}(t_k)| + (\mathbf{z}_S(t_k) - \mathbf{z}_{\mathcal{M}}(t_k))^T \mathbf{Q}_{\mathcal{M}}^{-1}(t_k)(\mathbf{z}_S(t_k) - \mathbf{z}_{\mathcal{M}}(t_k)) \right). \quad (43)$$

2.5.4 Comparison of the χ^2/Wishart distributions and multivariate Gaussian approaches for the likelihoods of the first two moments.

For the analysis of *CTT1* mRNA, the extension of the moments analyses to include the third and fourth moments led to identification of parameters that were $10^{93,900}$ times less likely to account for the full

measured mRNA distributions compared to the analysis using the FSP analysis (Table S5 and Section 2.8). Moreover, this result was $10^{63,300}$ times less likely to account for the distribution data than was the model identified by the much simpler χ^2 approach (Table S5). Similar deleterious effects were observed for the spatial *STL1* and *CTT1* analyses, although inclusion of the third and fourth moments led to some improvement in the case of non-spatial *STL1* analysis, for which the skewness had the greatest effect as shown in Figs. 3 and S7.

Recall from the main text that the model is unable to fit the means and variances exactly due to the difficulty to estimate those statistics due to high skewness. In order to compensate for this mismatch, the extended first-four moments approach identifies very large 3rd and 4th moments. However, these higher moments are not directly constrained by the data, and they are severely over-estimated (as opposed to under estimated as they were in the χ^2 and Wishart distribution based approaches). As a result, the extended model provided excelent fits to the means, but fits to all other statistics are much worse as shown in Fig. S6. In principle, this could be corrected by using data from the 3rd and 4th moments to add additional constraints to the model, but such an approach would be problematic for two reasons: (1) the measurement of the 3rd and 4th moments are prone to even greater sampling error than are the first two moments; and (2) in order to compute the likelihood to observe the third and fourth moments requires computation of even higher moments, which increases the computational complexity and makes such analysis impractical for the current model.

Because the extended moments analysis requires greater computational effort to compute while providing worse predictions to the full distributions in most cases, we have restricted the majority of our discussion to the simpler moments-based analyses.

2.6   Likelihood to observe measured distributions

Because the FSP approach provides a direct computation of the model's probability distribution, the FSP-based computation of the likelihood of the measured data is much more straightforward, and it does not require any assumptions of the distributions' shapes. To define this likelihood function, suppose that n_c cells, $c = [1, 2, \ldots, n_c]$, were measured for a given experiment and time point, and each cell was found to have exactly $m_{\mathrm{nuc}}(c)$ copies nuclear mRNA and $m_{\mathrm{cyt}}(c)$ copies cytoplasmic mRNA. Suppose that a model with parameter set $\boldsymbol{\Lambda}$, predicts that for each time and experiment, the probability that a given cell has exactly $m_{\mathrm{nuc}}(c)$ nuclear mRNAs and $m_{\mathrm{cyt}}(c)$ in the corresponding conditions is $p(m_{\mathrm{nuc}}(c), m_{\mathrm{cyt}}(c)|\boldsymbol{\Lambda})$. The total likelihood of all observations, $L(\mathbf{D}|\boldsymbol{\Lambda})$, is the product over every cell, or

$$L(\mathbf{D}|\boldsymbol{\Lambda}) = \prod_{c=1}^{n_c} p(m_{\mathrm{nuc}}(c), m_{\mathrm{cyt}}(c)|\boldsymbol{\Lambda}). \tag{44}$$

Now that we know how likely it is that the data comes from a model and a given set of parameters, $\boldsymbol{\Lambda}$, our goal is to find the parameter set, $\boldsymbol{\Lambda}_{\mathrm{Fit}}$, which maximizes this likelihood (or equivalently the logarithm of this likelihood):

$$\boldsymbol{\Lambda}_{\mathrm{Fit}} = \mathrm{argmax}_{\boldsymbol{\Lambda}} \log(L(\mathbf{D}|\boldsymbol{\Lambda})) \tag{45}$$

$$= \mathrm{argmax}_{\boldsymbol{\Lambda}} \sum_{c=1}^{n_c} \log p(m_{\mathrm{nuc}}(c), m_{\mathrm{cyt}}(c)|\boldsymbol{\Lambda}). \tag{46}$$

Under the assumption that cells are independent, and because each cell is measured only once using the smFISH technique, the log-likelihood that the model matches all experiments at all time points is the sum of the log-likelihoods of the individual experiments and time points.

2.7   Parameter searches to maximize likelihood

In order to conduct parameter searches, we use iterative combinations of simplex based searches (e.g., MATLAB's "fminsearch" function) and genetic algorithm based searches. All parameters were defined to have positive values, and searches were conducted in logarithmic space. The searches are run multiple times from different starting parameter guesses leading to many tens of millions of function evaluations ($> 4 \times 10^7$ evaluations of the means and moments analyses, $> 5 \times 10^6$ evaluations of the non-spatial FSP distributions, and $> 1 \times 10^6$ evaluations for the more computationally expensive analyses of extended moments and the spatial FSP distributions). Parallel fits were conducted on clusters of more than 128 processors at a time allowing for the consideration of several millions of model/ parameter/ experiment combinations per day.

2.8   Comparison of results for different likelihood functions (Table S5)

Table S5 shows the relative log-likelihood values for different likelihoods that compare the means, means and variances, extended moments, or full distributions. Each row corresponds to a different combination of gene and identification strategy. Each column corresponds to a different likelihood function (i.e., means, means and (co)variances, extended moments, or full distributions). Values presented are $\log_{10}$ of the actual likelihoods relative to the best value found for that specific objective function.

The 'Distributions' *column* of Table S5 quantifies the relative log-likelihood that the identified parameter set matches *all data* of that type (i.e., spatial or nonspatial). More negative numbers denote worse matches to the full data. For example, in the non-spatial analysis of *CTT1*, the χ^2 and extended moments-based approaches were respectively $10^{30,600}$ and $10^{93,900}$ times less likely to account for the full data than was the model identified by the FSP approach. In other words, the full data was $10^{63,300}$ times less likely to have come from the model identified using the extended moments than it was to have come from the simpler χ^2-based analysis.

The Full FSP distributions *row* of Table S5 shows the relative likelihood of the Full FSP Distribution parameters when compared to the best fit for each of the different likelihood functions. This quantity provides an estimate of the probability that each likelihood function would have discovered the FSP parameters by chance. One interesting observation from this perspective is that although the extended moments analyses produce worse fits to the full data, this effect is somewhat mitigated by the fact that the extended analysis yields greater uncertainties (see also Figs. 4B, S8-S10). In other words, the extended analysis leads to worse fits to the full data, but this is coupled with lower confidence in these poor results.

2.9   Metropolis Hastings algorithm to quantify parameter uncertainties

To quantify the parameter uncertainties, we used the Metropolis Hastings algorithm [12], which is a standard Markov Chain Monte Carlo (MCMC) algorithm for parameter uncertainty estimation. All MCMC parameter explorations were conducted in logarithmic parameter space, and all analyses (i.e., means, means and variances, or distributions, both spatial and non-spatial) used the same proposal distribution for the MCMC chains. This proposal distribution was a symmetric normal distribution (in logarithmic space) with a variance of 0.005 (also in logarithmic space). For each parameter proposal, a random selection of parameters were selected to change, where each parameter had a 50% chance to be perturbed. The first half of each chain was discarded as an MCMC burnin period, and all chains were thinned by 90%.

2.9.1   Convergence

MCMC chains for the means, simpler moments analyses, and non-spatial FSP analyses were run for MH chains with combined lengths of $>25,000,000$ parameter evaluations. MCMC analyses for the more

computationally expensive extended moment analyses were run for combined lengths of $>$1,500,000 parameter evaluations. MCMC analyses for the most computationally expensive spatial distribution analyses were run for a combined length of $>$3,700,000 parameter evaluations. To evaluate convergence of the MCMC analyses, we have split the multiple MCMC chains into two disjoint sets. To illustrate the achieved convergence, Figures S8 shows the distributions of likelihood values for these two independent MCMC compilations for each analysis and for *STL1* and *CTT1*. Thus, all 32 MHA analyses (2 replicas $\times$ 2 genes $\times$ 4 statistical analyses $\times$ 2 spatial analyses) were confirmed to have sampled similar distributions of log-likelihood space.

2.9.2 MCMC Results

Figures S9 and S10 summarize the biases and pairwise parameter uncertainties for the *STL1* and *CTT1* analyses and for each of the eight different analyses (means, means and variances, extended moments, and distributions)$\times$(spatial and non-spatial).

The vectors in Figs. S9 and S10 represent the fold over- or under-estimation bias for the corresponding parameter. The matrices in Figs. S9 and S10 represent the variances (diagonal entries) and covariances (off-diagonal entries) of the parameter estimation uncertainty, as estimated using the Metropolis Hastings algorithm. For example, the figure shows that non-spatial means analysis overestimates the k_{i_3} and γ parameters ('+' symbols in the corresponding biases), is highly uncertain in the estimate of k_{i_3} (yellow box in the covariance matrix diagonal corresponding to that parameter), and the uncertainties in parameters k_{i_3} and γ are positively correlated ('+' symbol in corresponding off-diagonal entries of the covariance matrix). The open red ellipse plotted in Figs. 4A visually depicts the same information by plotting the 90% confidence parameter interval, assuming a lognormal posterior distribution with the MCMC-estimated pairwise covariance matrix.

The *total bias* shown in Figs. 4C and S11C was defined by the euclidean distance in logarithmic space according to the expression:

$$d_{\text{bias}} \equiv 10^{\sqrt{\sum \left[\log_{10}\left(\frac{\lambda_i}{\tilde{\lambda}_i}\right)\right]^2}}, \tag{47}$$

where $\{\lambda_i\}$ is the average of the ith estimated parameter, and $\{\tilde{\lambda}_i\}$ is the corresponding 'true' parameters (i.e., the maximum likelihood estimate using all data and the spatial FSP analysis). The summation is taken over all parameters *except* $k_{21}^{(0)}$ and $k_{21}^{(1)}$, which provide a non-unique determination of the Hog1p saturation effect, k_{i_1}, which is nearly zero and therefore highly uncertain in logarithmic space, and t_0 whose interpretation is different for the spatial and non-spatial models. Conceptually, the value d_{bias} provides a quantification of the overall $\pm$ fold changes for the collective parameters compared to their 'true' values.

The *total uncertainty* shown in Figs. 4B and S11B was defined by the trace of the covariance matrix. As was the case for the total bias quantification, the trace is taken over all parameters *except* $k_{21}^{(0)}$, $k_{21}^{(1)}$, k_{i_1}, and t_0.

2.10 Fisher Information analysis

The Fisher Information Matrix (FIM), $\mathcal{I}(\Lambda)$, and its inverse, the Cramér-Rao bound, is an analysis technique that describes the lower bound on the variance of an unbiased estimator. Recent works [7, 13, 14] have applied this tool in a biological context, looking at model sensitivity, robustness, identifiability, and experiment design. Here, we are concerned with the ability to identify models, which (1) only consider the means or the means and variances, and (2) assume a Gaussian likelihood function for the sample means

and variances. The FIM is defined for the parameter vector $\boldsymbol{\Lambda} \equiv [\lambda_1, \lambda_2, ..., \lambda_p]$ and likelihood $L(\mathbf{D}|\boldsymbol{\Lambda})$ as

$$\mathcal{I}(\boldsymbol{\Lambda}) = \mathbb{E}\left\{\left(\nabla_{\boldsymbol{\Lambda}} \log L(\mathbf{D}|\boldsymbol{\Lambda})\right)^T \left(\nabla_{\boldsymbol{\Lambda}} \log L(\mathbf{D}|\boldsymbol{\Lambda})\right)\right\}. \tag{48}$$

In this work, we have compared parameter uncertainties using posterior distributions of the parameters. The Cramér-Rao inequality states that the variances of these distributions must be less than or equal to the inverse of the FIM, $\mathcal{I}(\boldsymbol{\Lambda})^{-1}$. A model is unidentifiable if $\mathcal{I}(\boldsymbol{\Lambda})^{-1}$ does not exist, i.e. if the FIM is singular [15].

For the models that consider means $\boldsymbol{\mu}$, means and variances, $\boldsymbol{\mu}$ and $\boldsymbol{\Sigma}$, we have assumed Gaussian forms of the likelihood function, Eqns. 28 and 38. Under this assumption, the FIM is well-known. For a model which only describes the mean of the distribution, it is given by

$$\mathcal{I}(\boldsymbol{\Lambda})^{\boldsymbol{\mu}}_{i,j} = \mathbb{E}\left(\frac{\partial \boldsymbol{\mu}}{\partial \lambda_i}\right)^T \boldsymbol{\Sigma}_S^{-1} \left(\frac{\partial \boldsymbol{\mu}}{\partial \lambda_j}\right), \tag{49}$$

and when both means and variances are to be estimated with the model, the FIM is

$$\mathcal{I}(\boldsymbol{\Lambda})^{\boldsymbol{\mu},\boldsymbol{\Sigma}}_{i,j} = \mathbb{E}\left\{\left(\frac{\partial \boldsymbol{\mu}}{\partial \lambda_i}\right)^T \boldsymbol{\Sigma}_{\mathcal{M}}^{-1} \left(\frac{\partial \boldsymbol{\mu}}{\partial \lambda_j}\right) + \frac{1}{2}\text{trace}\left(\boldsymbol{\Sigma}_{\mathcal{M}}^{-1}\frac{\partial \boldsymbol{\Sigma}_{\mathcal{M}}}{\partial \lambda_i}\boldsymbol{\Sigma}_{\mathcal{M}}^{-1}\frac{\partial \boldsymbol{\Sigma}_{\mathcal{M}}}{\partial \lambda_j}\right)\right\}. \tag{50}$$

Given a set of independent samples at each experimentally measured time point, the FIM can be constructed at each time point by integrating Eqns. 11 and 12, and the total information is the sum over all the time points. For models of $\boldsymbol{\mu}$ and $\boldsymbol{\mu}$ and $\boldsymbol{\Sigma}$, we computed the FIM and found that them to be invertible, indicating that the parameters are in principle able to be identified.

2.11 Predictions of Transcription Site activity

We developed two analyses to predict transcription site (TS) activity: a simplified theoretical analysis of average active TS activity and an extended FSP analysis of distributions of polymerases on a given TS. These are described below. For both the data and the model, TS sites were considered to be ON if their predicted or measured intensities were greater than twice the intensity of a single mature mRNA.

2.11.1 Simplified theoretical model of average TS polymerase loading

Using the mRNA distribution analyses described above, we identified transcription initiation rates, $\{k_{i_1}, k_{i_2}, k_{i_3}, k_{i_4}\}$ for the *CTT1* and *STL1* mRNA. For an elongation rate of k_{elong} and an mRNA length of L, each polymerase takes a time of $\tau_{\text{elong}} = L/k_{\text{elong}}$ to complete transcription. Thus, polymerases that initiate transcription in the time window $(t - \tau_{\text{elong}}, t)$ will be present at the TS at time t. For each gene, we selected the fastest identified transcription rate $k_{\text{i}-\max} = \max\{k_{i_1}, k_{i_2}, k_{i_3}, k_{i_4}\}$. Assuming that an *active* TS is in the state with the maximum transcription rate, the average number of polymerases per active TS, $\langle n_{\text{pol}}\rangle$, can be computed as:

$$\langle n_{\text{pol}}\rangle = k_{\text{i}-\max}\tau_{\text{elong}} = \frac{k_{\text{i}-\max}L}{k_{\text{elong}}}. \tag{51}$$

In practice, L was chosen as the length from the first smFISH probe on the 5' end of the mRNA to the transcription termination site. In light of the fact that the smFISH probes are nearly equally distributed along the mRNA, we assume that nascent mRNA are on average half the length of their mature counterparts. Under this assumption we related $n_{\text{pol}} = 2n_{\text{nascent}}$, which allows us to relate the elongation rate to the observed spot intensities (in terms of mature mRNA) as:

$$\left\langle \frac{I_{\text{TS}}}{I_{\text{mature}}}\right\rangle = \langle n_{\text{nascent}}\rangle = \frac{k_{\text{i}-\max}L}{2k_{\text{elong}}}. \tag{52}$$

17

2.11.2 Extended FSP model of nascent transcription

Next, we extended Finite State Projection approach in a form similar to that in [16]. To compute the distribution for the number of polymerases at the TS, we first compute the distribution of the gene states at the earlier time, $t - \tau_{\text{elong}}$. Using this distribution of gene states at $t - \tau_{\text{elong}}$ and ignoring previous initiation events and excluding degradation of partially described mRNA, we use the FSP analysis derived above (but with no degradation or transport) to solve for the distribution of elongating polymerases per TS at the time t. We assume that each partially transcribed mRNA is at a random location in the gene, and it therefore has an effective intensity uniformly distributed between zero and the equivalent of one mRNA. To find the distribution of TS spot intensities with N_{poly} polymerases, we take the convolution of N_{poly} independent random variables, each with a uniform distribution between zero and one.

To confirm the FSP analysis, we also simulated the identified models using an adapted form of the Stochastic Simulation Algorithm (SSA, [17]) but with a modification similar to that proven in [18]. In each run of the SSA, we recorded the times of every simulated transcription initiation event. With this simulated information and an assumption of deterministic mRNA elongation with a given elongation rate, we compute the distance traveled by each polymerase as a function of time. If that length is longer than the length of the gene, then that polymerase is assumed to have completed transcription, in which case the mRNA is assumed to have dissociated from the TS. Otherwise, the length of the elongating mRNA and the known smFISH probe placements (Table S1) are used to determine how many probes are located along the partially transcribed nascent mRNA for that particular polymerase. The total TS intensity is then computed as the sum of the intensities for all polymerases on the gene in that cell and at that point in time.

The standard SSA approach [17] assumes constant propensity functions. In order to allow for time varying rates in the propensity functions (i.e., Eqn. 2), we added a fast reaction to the system. The stoichiometry of this reaction was zero, such that each firing of this null reaction does not affect the state of the system [18], but it does allow for frequent updates to the propensity functions. The rate of this reaction was set to $1s^{-1}$, which is more than two orders of magnitude faster than the characteristic rates of the Hog1p fluctuations in Eqn. 1. Figure S12 shows excellent agreement between the FSP and SSA analysis of the TS activity for *STL1* and *CTT1* transcription under 0.2M and 0.4M NaCl osmotic shock conditions.

2.11.3 Identification of mRNA elongation rate

In order to identify the transcription elongation rate, we computed the TS intensity distribution for *CTT1* at each point in time for 0.2M and 0.4M NaCl osmotic shock using the previously identified parameters (Table S4) and one free constant to describe the average elongation rate, k_{elong}. We then computed the probability that the observed distributions of *CTT1* TS intensities could have originated from this model at all time points and conditions. We then maximized this likelihood with respect to the rate k_{elong} for the different experimental replicas and NaCl concentrations to determine the uncertainty in this parameter. Using the simplified theoretical model, which does not account for transitions between active and inactive periods, we found an *upper bound* on the *CTT1* elongation rates to be 91±9Nt/s. Using the more detailed spatial FSP approach, we found the *CTT1* elongation rates to be 63±14Nt/s. For both cases, the uncertainty is given as the standard error of the mean using the five experimental replicas (two for 0.2M NaCl and three for 0.4M NaCl). We then fixed the elongation rate to be 63Nt/s, and we used this rate in conjunction with the previously identified parameters to predict the TS intensity distributions for *CTT1* and *STL1* as functions of time in both osmotic shock conditions (Figs. 4D and S11D-H).

Supplemental References

[1] D. Muzzey, C. A. Gómez-Uribe, J. T. Mettetal, A. van Oudenaarden. 'A Systems-Level Analysis of Perfect Adaptation in Yeast Osmoregulation'. *Cell*, **138**(1):160–171, 2009.

[2] P. Ferrigno, F. Posas, D. Koepp, H. Saito, P. A. Silver. 'Regulated nucleo/cytoplasmic exchange of HOG1 MAPK requires the importin β homologs NMD5 and XPO1'. *Embo J.*, **17**(19):5606–5614, 1998.

[3] A. D. Edelstein, M. A. Tsuchida, N. Amodaj, H. Pinkard, R. D. Vale, N. Stuurman. 'Advanced methods of microscope control using μManager software'. *Journal of Biological Methods*, **1**(2):e10, 2014.

[4] J. T. Mettetal, D. Muzzey, C. Gomez-Uribe, A. van Oudenaarden. 'The Frequency Dependence of Osmo-Adaptation in Saccharomyces cerevisiae'. *Science*, **319**(5862):482–484, 2008.

[5] G. Neuert, B. Munsky, R. Z. Tan, L. Teytelman, M. Khammash, A. van Oudenaarden. 'Systematic Identification of Signal-Activated Stochastic Gene Regulation'. *Science*, **339**(6119):584–587, 2013.

[6] J. P. Hespanha, A. Singh. 'Stochastic models for chemically reacting systems using polynomial stochastic hybrid systems'. *International Journal of robust and nonlinear control*, **15**(15):669–690, 2005.

[7] J. Ruess, A. Milias-Argeitis, J. Lygeros. 'Designing experiments to understand the variability in biochemical reaction networks'. *Journal of The Royal Society Interface*, **10**(88):20130588–20130588, 2013.

[8] D. McQuarrie. 'Stochastic Approach to Chemical Kinetics'. *J. Applied Probability*, **4**:413–478, 1967.

[9] B. Munsky, M. Khammash. 'The Finite State Projection Algorithm for the Solution of the Chemical Master Equation'. *The Journal of Chemical Physics*, **124**(4):044104, 2006.

[10] B. Munsky, M. Khammash. 'The Finite State Projection Approach for the Analysis of Stochastic Noise in Gene Networks'. *IEEE Trans. Automat. Contr./IEEE Trans. Circuits and Systems: Part 1*, **52**(1):201–214, 2008.

[11] J. Wishart. 'The Generalised Product Moment Distribution in Samples from a Normal Multivariate Population'. *Biometrika*, **20A**(1/2):32, 1928.

[12] S. Chib, E. Greenberg. 'Understanding the Metropolis-Hastings Algorithm'. *The American Statistician*, **49**(4):327–335, 1995.

[13] M. Komorowski, M. J. Costa, D. A. Rand, M. P. H. Stumpf. 'Sensitivity, robustness, and identifiability in stochastic chemical kinetics models.' *Proceedings of the National Academy of Sciences*, **108**(21):8645–8650, 2011.

[14] C. Zimmer. 'Experimental Design for Stochastic Models of Nonlinear Signaling Pathways Using an Interval-Wise Linear Noise Approximation and State Estimation'. *PloS one*, **11**(9):e0159902, 2016.

[15] T. J. Rothenberg. 'Identification in Parametric Models'. *Econometrica*, **39**(3):577–591, 1971.

[16] A. Senecal, B. Munsky, F. Proux, N. Ly, F. E. Braye, C. Zimmer, F. Mueller, X. Darzacq. 'Transcription factors modulate c-Fos transcriptional bursts.' *Cell Reports*, **8**(1):75–83, 2014.

[17] D. T. Gillespie. 'Exact stochastic simulation of coupled chemical reactions'. *J. Phys. Chem.*, **81**:2340–2361, 1977.

[18] M. Voliotis, P. Thomas, R. Grima, C. G. Bowsher. 'Stochastic Simulation of Biomolecular Networks in Dynamic Environments'. *arXiv:1511.01268*, 2015.
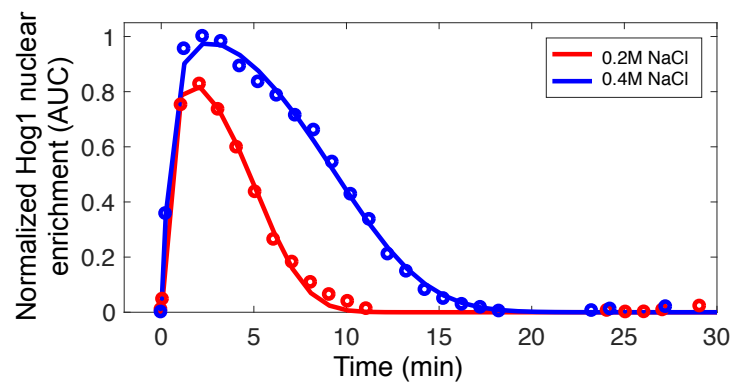
Figure S1: Normalized Hog1 nuclear enrichment after activation of the HOG-pathway with different NaCl concentrations. Solid lines denote the model (Eqns. 1) fit to the data points (symbols) for the two different osmolyte concentrations.
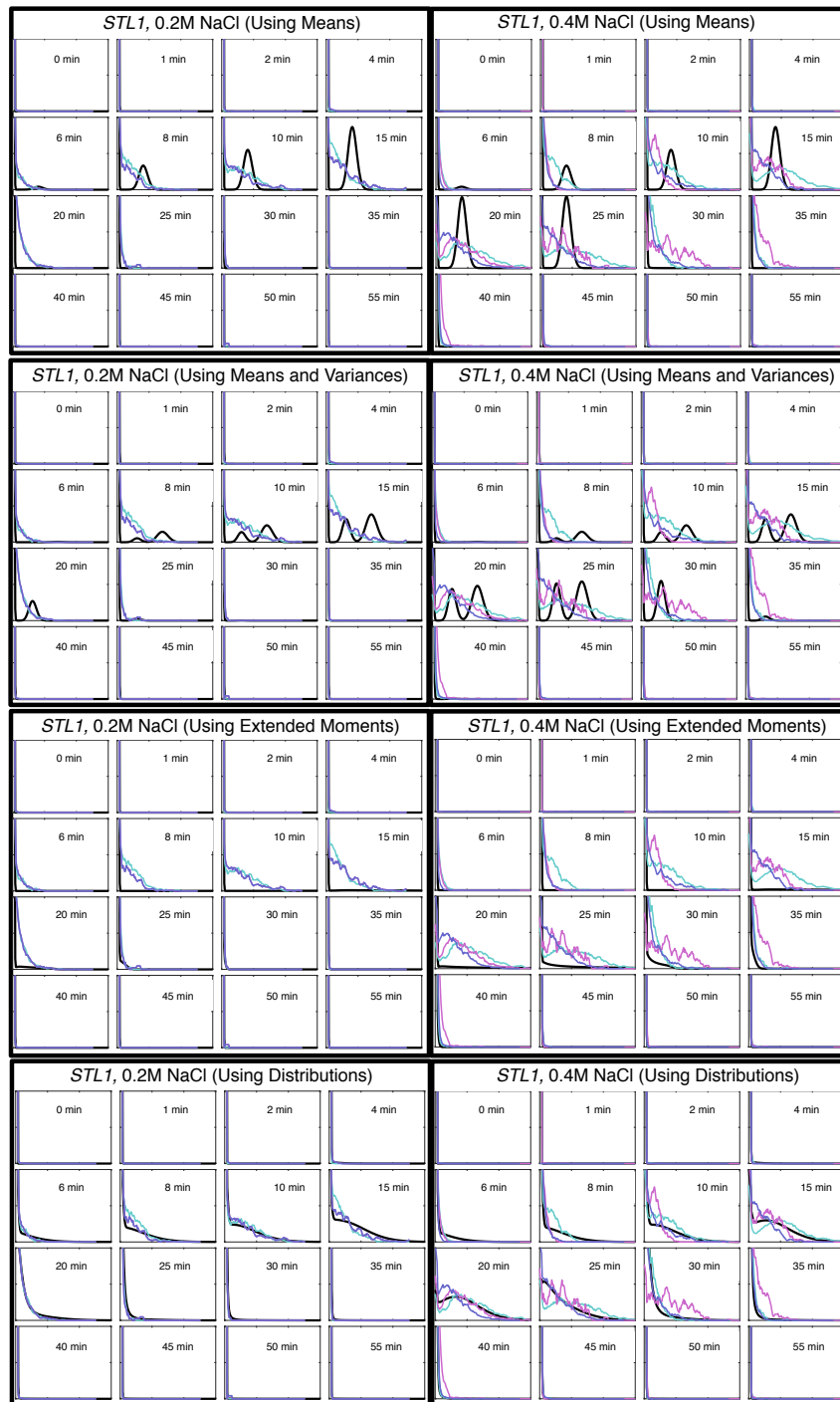
Figure S2: Experimental and model-generated distributions for the number of *STL1* per cell versus time for 0.2M NaCl (left) and 0.4M NaCl (right) osmotic shocks. Distributions have been generated using the models identified using means only (top row), means and variances using the χ^2 approach (second row), means and variances using the extended moments analysis (third row) or full distributions (bottom row). Model results are shown in black. Experimental data replicates shown in colors. Limits of all x-axes are 0 to 150 copies of mRNA. Limits of all y-axes are probability mass of 0 to 0.04.

22
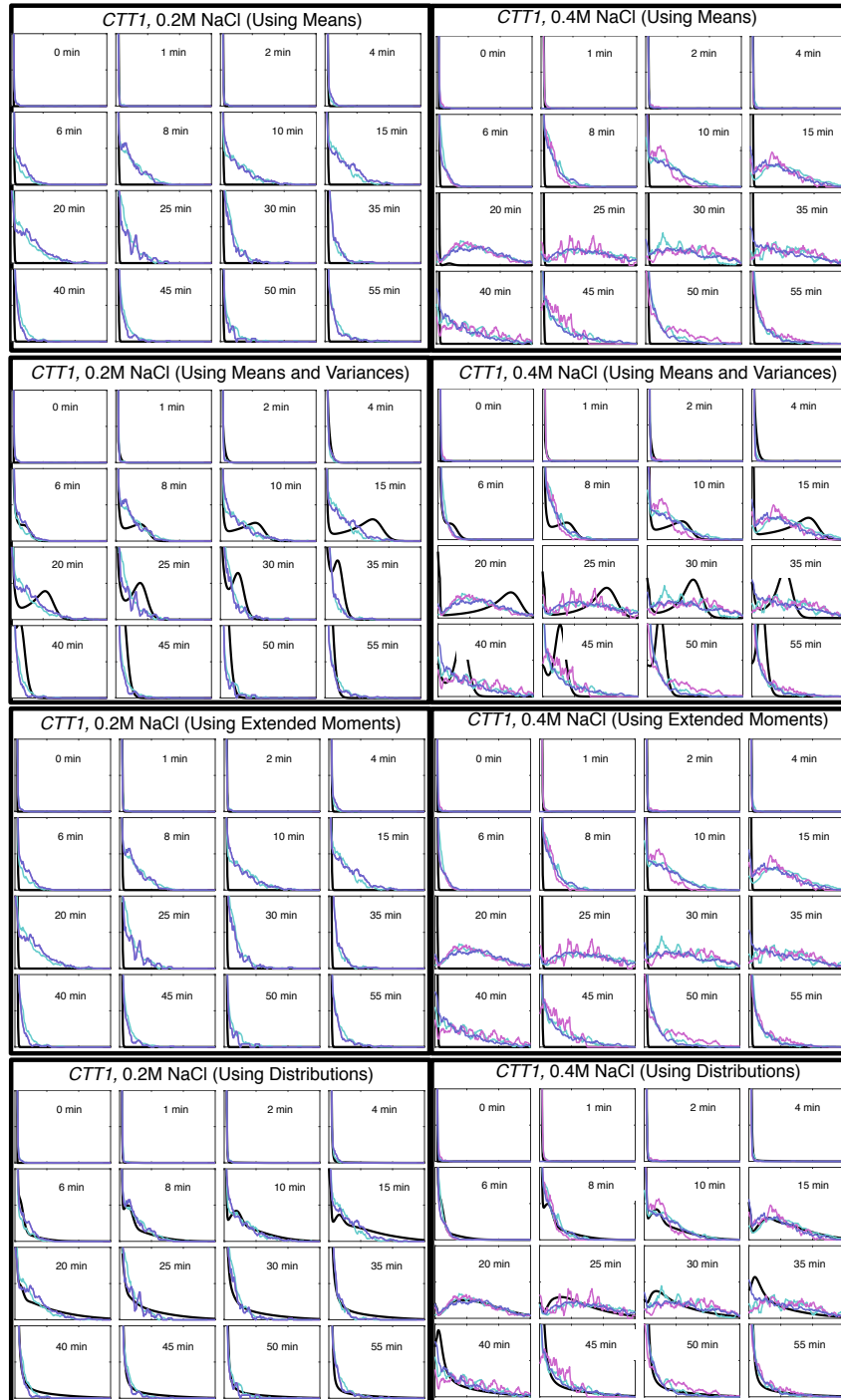
Figure S3: Experimental and model-generated distributions for the number of *CTT1* per cell versus time for 0.2M NaCl (left) and 0.4M NaCl (right) osmotic shocks. Distributions have been generated using the models identified using means only (top row), means and variances using the χ^2 approach (second row), means and variances using the extended moments analysis (third row) or full distributions (bottom row). Model results are shown in black. Experimental data replicates shown in colors. Limits of all x-axes are 0 to 150 copies of mRNA. Limits of all y-axes are probability mass of 0 to 0.04.
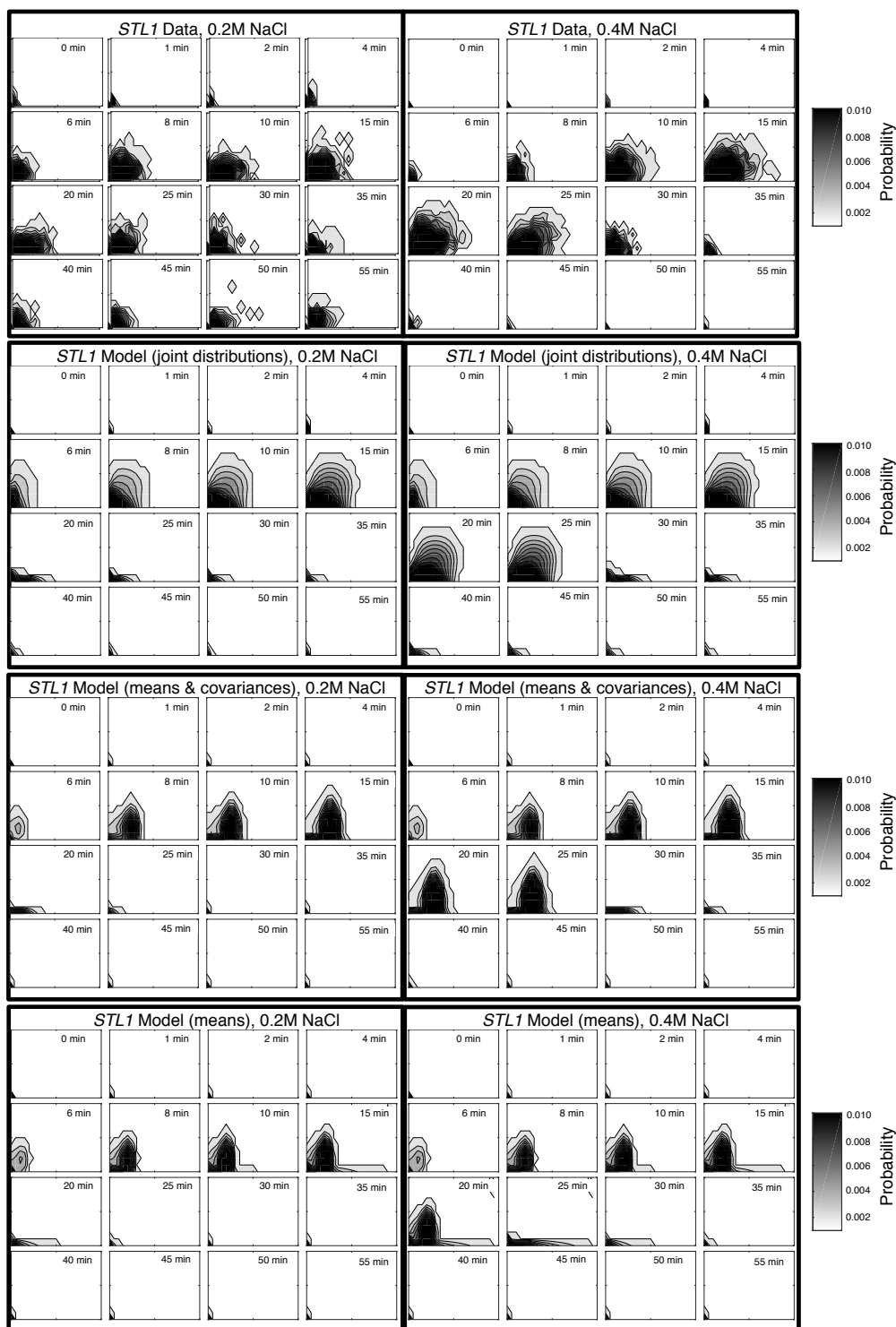
Figure S4: Experimental (top) and model-generated (bottom) joint distributions for *STL1* versus time for 0.2M NaCl (left) and 0.4M NaCl (right) osmotic shocks. Distributions have been generated using the model identified from the full joint distributions (row 2), the means and covariances (row 3) or the joint means (row 4). Limits of all x-axes are 0 to 200 copies of cytoplasmic mRNA. Limits of all y-axes are 0 to 10 copies of nuclear mRNA. All plots use the same contour levels (see legend to right). See Table S3 for the corresponding parameter sets.
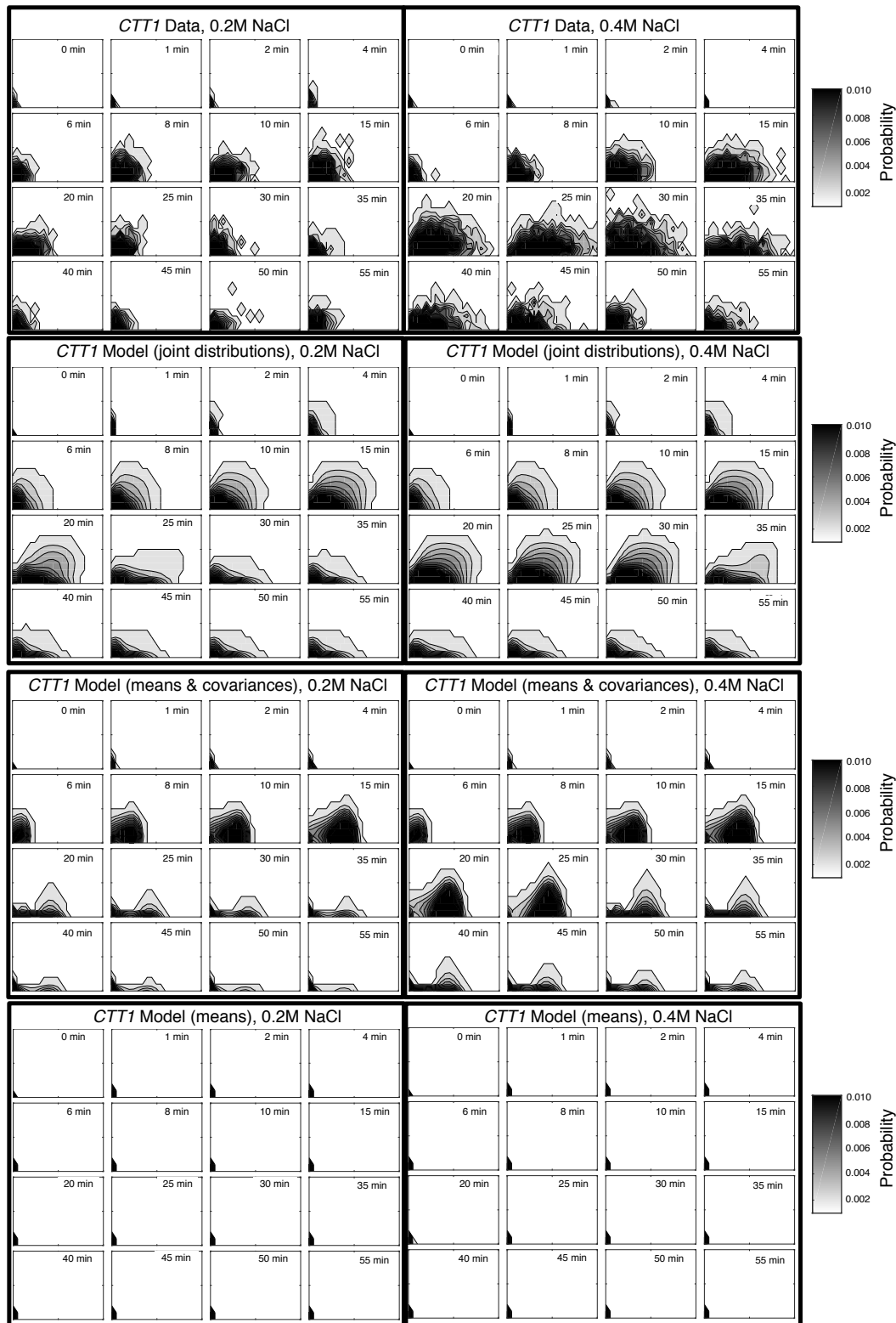
Figure S5: Experimental (row 1) and model-generated (rows 2-4) joint distributions for *CTT1* versus time for 0.2M NaCl (left) and 0.4M NaCl (right) osmotic shocks. Distributions have been generated using the model identified from the full joint distributions (row 2), the means and covariances (row 3) or the joint means (row 4). Limits of all x-axes are 0 to 200 copies of cytoplasmic mRNA. Limits of all y-axes are 0 to 10 copies of nuclear mRNA. All plots use the same contour levels (see legend to right). See Table S4 for the corresponding parameter sets.
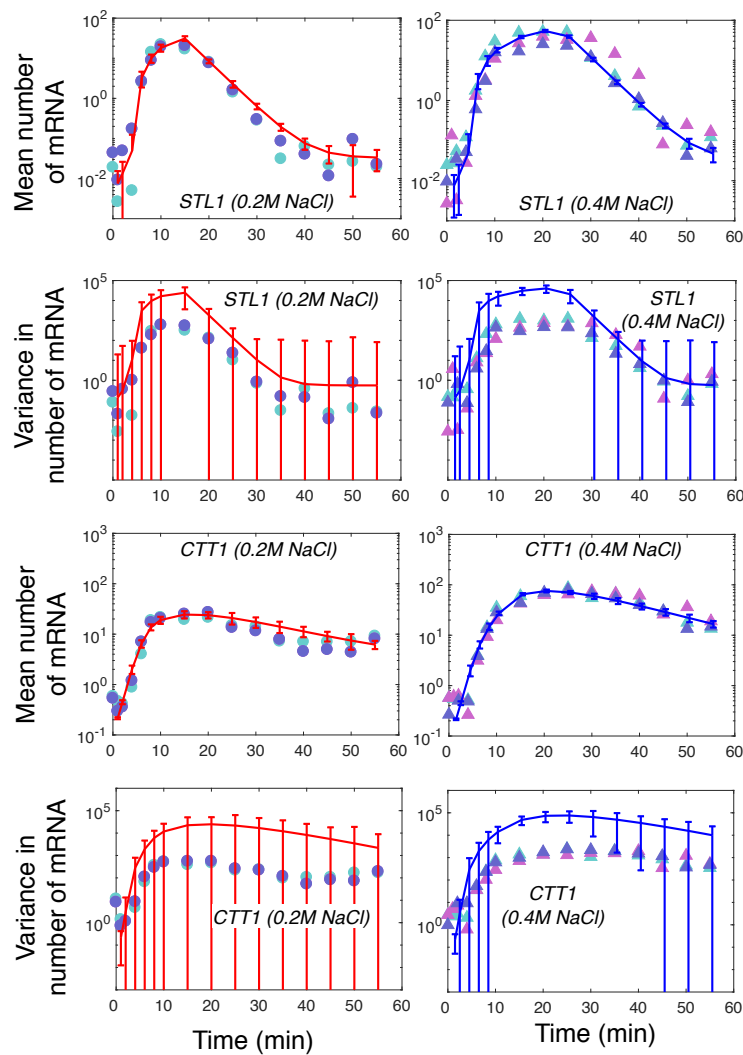
Figure S6: Best fit to the means and variances using the extended moments analysis for *STL1* and *CTT1* for 0.2M NaCl (left, 2 biological replica) and 0.4M NaCl (right, three biological replica) osmotic shock. Error bars denote the expected errors of one standard error above and below the estimated value for the corresponding statistic. According to the likelihood function defined in Section 2.5.3.4, the standard error of the sample mean is given by $\sqrt{\sigma_{11}/N_S}$, and the standard error of the sample variance is given by $\sqrt{(\sigma_{1111} - \frac{N_S-3}{N_S-1}\sigma_{11}^2)/N_S}$, where N_S is the sample size corresponding to the total measured number of cells for that time point and condition). Experimental data replicates are shown by the circles and triangles.
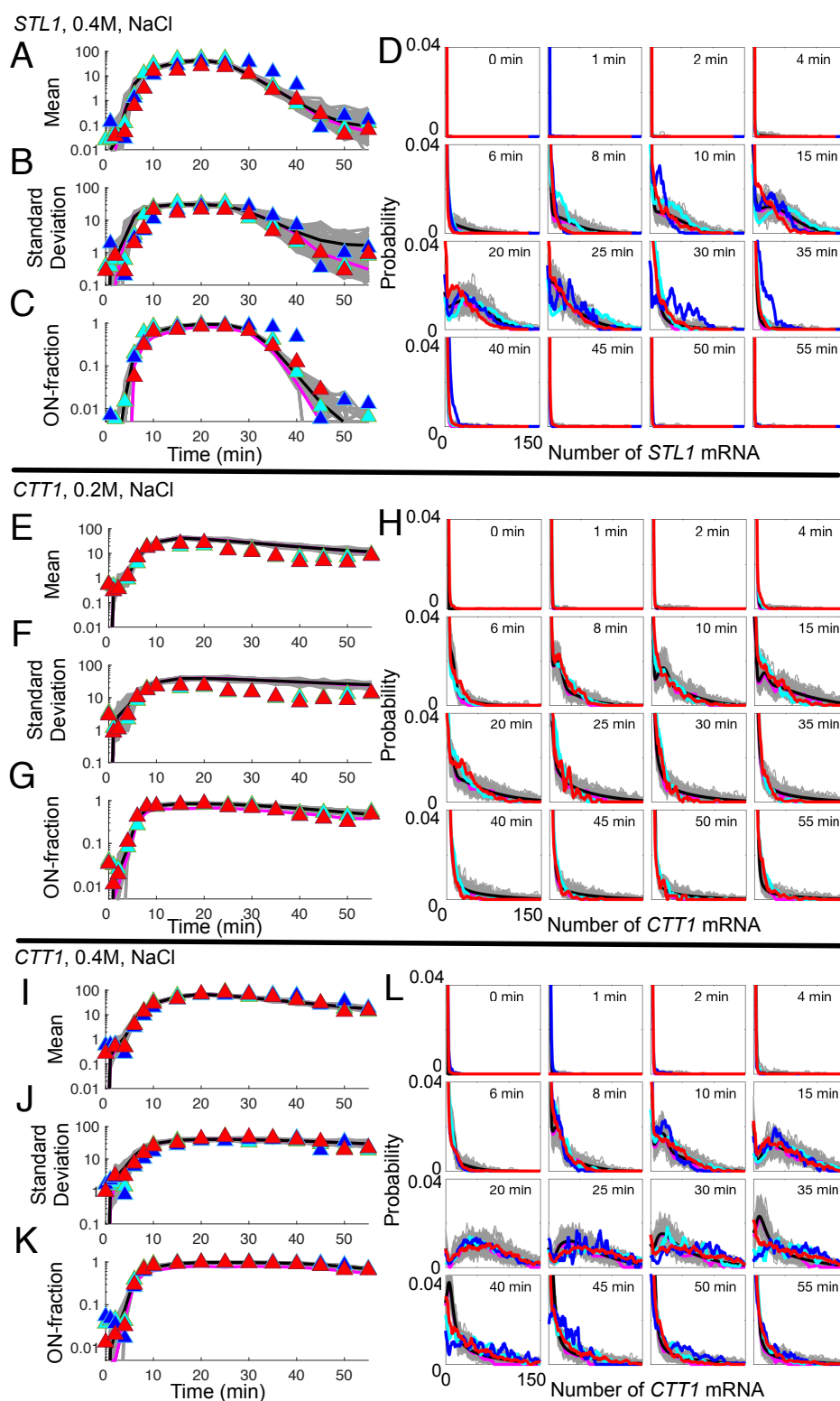
Figure S7: Means (A,E,I), standard deviations (B, F, J), ON-fractions (C, G, K) and probability distributions (D, H, L) for *STL1* at 0.4M NaCl osmotic shock (A-D), *CTT1* at 0.2M NaCl osmotic shock (E-H), and *CTT1* at 0.4M NaCl osmotic shock (I-L). In all panels, theoretical values from the fitted model are in black, representative simulated samples of 200 cells apiece are in gray, median statistics of the simulated samples are in magenta; and experimental data are in red and cyan (and blue for 0.4M NaCl). See also Figure 3 in the main text.
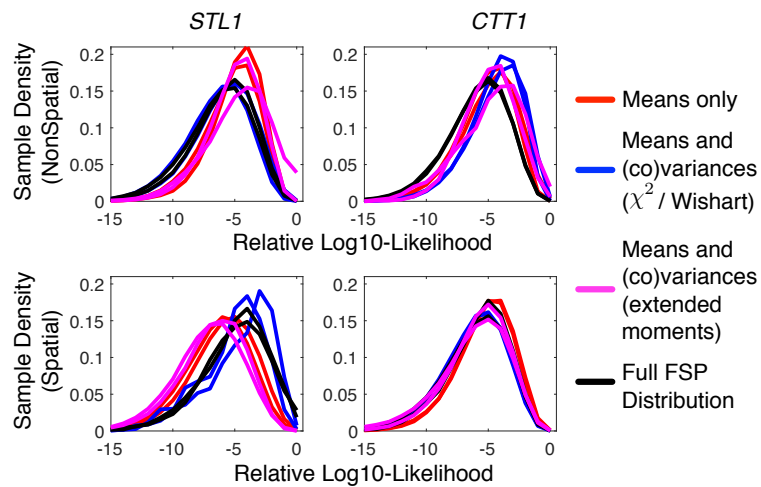
Figure S8: Distributions of $\log_{10}$-likelihoods that have been sampled by the Metropolis Hastings analysis for *STL1* (left) and *CTT1* (right) using non-spatial (top) or spatial (bottom) analyses. All likelihoods values are relative to the most likely model under the corresponding analysis. To illustrate convergence, multiple MH chains have been run for each analysis using means only (red, $> 1.2 \times 10^6$ MH samples per chain), means and variances using the χ^2 or Wishart approach (blue, $> 1.0 \times 10^6$ MH samples per chain), means and variances using the extended moments approach (magenta, $> 3.0 \times 10^5$ MH samples per chain), or distributions (black, $> 1.4 \times 10^5$ MH samples per chain for non-spatial analyses and $> 2.0 \times 10^4$ MH samples per chain for spatial analyses).

Figure S9: **Bias and Uncertainty in the estimation of parameters for the *STL1* mRNA transcription.**
MCMC results are summarized for the means (top row), means and variances using the χ^2 or Wishart approach (second row), means and variances using the extended moments analysis (third row), or full FSP distributions (bottom row) using non-spatial (left) or spatial (right) models. For each of the eight panels, the top row illustrates the parameter estimation biases, where the colors denote the fold-change magnitude of the estimation error (in logarithmic scale). Blue boxes represent well estimated parameters and yellow boxes represent poorly estimated parameters. The signs in each box denote whether the parameter is over estimated (+) or underestimated (-). The matrices at the bottom of each panel illustrate the joint uncertainties in all parameter combinations. These are shown in a logarithmic scale from low variance (blue) to high variance (yellow). The signs in each box denote whether the corresponding parameter combination is positively or negatively correlated. The same color scale is used in all panels to illustrate the relative effects of uncertainty and bias for the different analyses. The entries boxed in red correspond to the parameter ellipses for k_{i3} and γ, which are shown in Fig. 4A.
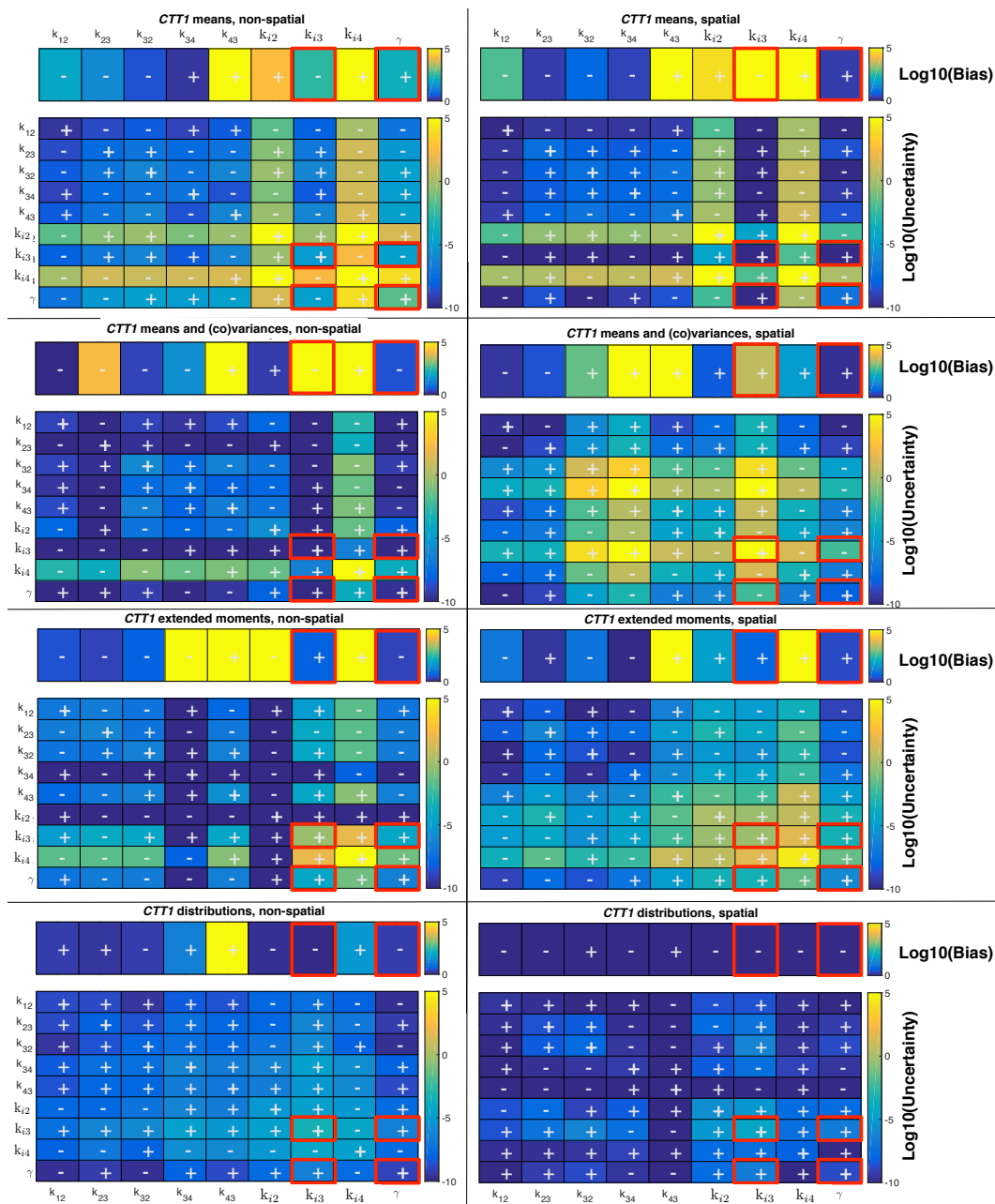
Figure S10: **Bias and Uncertainty in the estimation of parameters for the *CTT1* mRNA transcription.** MCMC results are summarized for the means (top row), means and variances using the χ^2 or Wishart approach (second row), means and variances using the extended moments analysis (third row), or full FSP distributions (bottom row) usin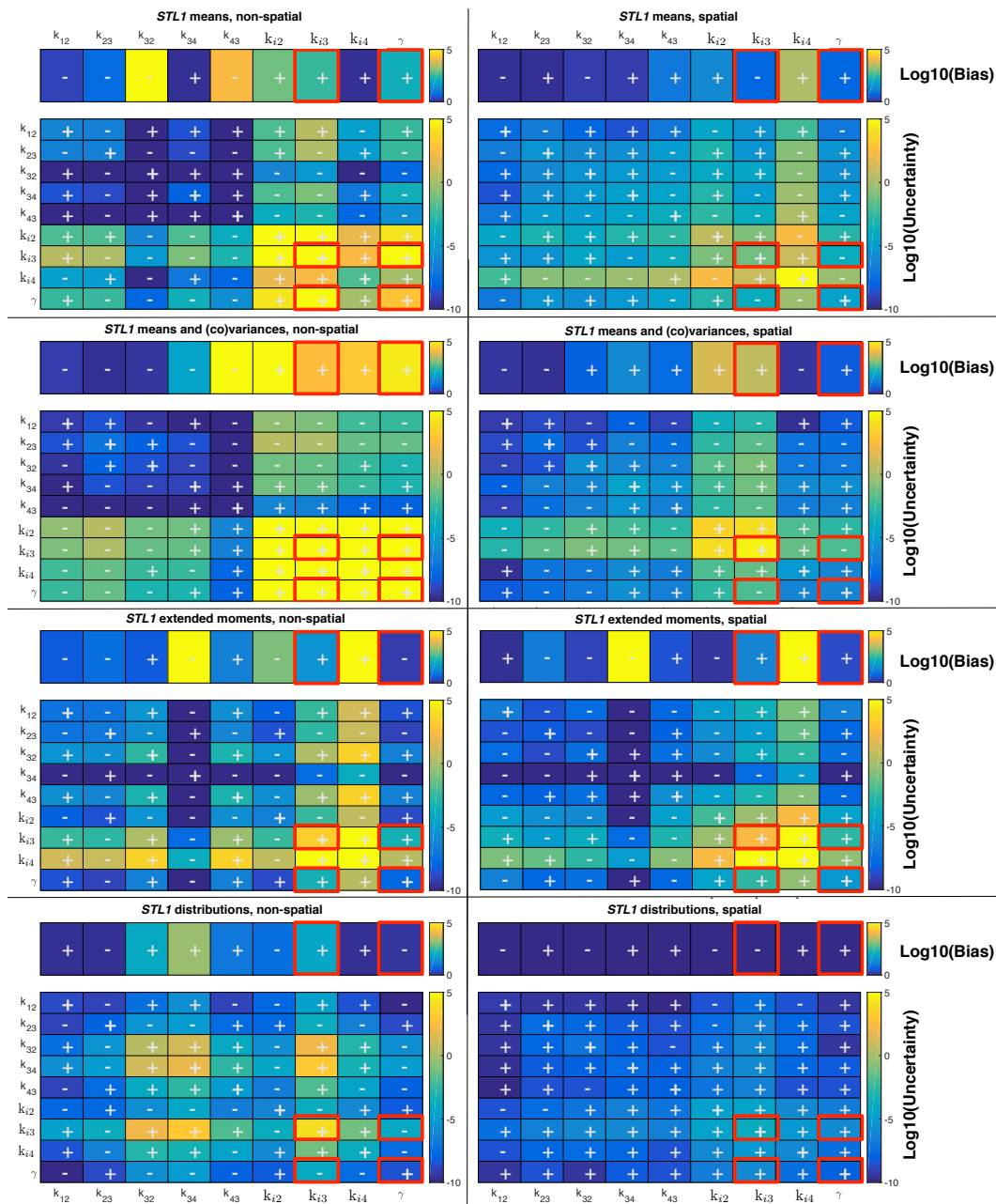g non-spatial (left) or spatial (right) models. For each panel, the top row illustrates the parameter estimation biases, where the colors denote the fold-change magnitude of the estimation error (in logarithmic scale). Blue boxes represent well estimated parameters and yellow boxes represent poorly estimated parameters. The signs in each box denote whether the parameter is over estimated (+) or underestimated (-). The matrices at the bottom of each panel illustrate the joint uncertainties in all parameter combinations. These are shown in logarithmic scale from low variance (blue) to high variance (yellow). The signs in each box denote whether the corresponding parameter combination is positively or negatively correlated. The same color scale is used in all six panels to illustrate the relative effects of uncertainty and bias for the six different analyses. The entries boxed in red correspond to the parameter ellipses for k_{i3} and γ, which are shown in Fig. S11A.

Predicted Numbers of Nascent *CTT1* Transcripts per Active Transcription Site (mRNA/TS)		
	Nonspatial	Spatial
Means only	3,700,000	3,500,000
Means and (co)variances (with χ^2/Wishart)	4,600	15,000
Extended moments	10,000	4,600
Full FSP distributions	5.7	5.1
Experimental result	3.7–7.1	
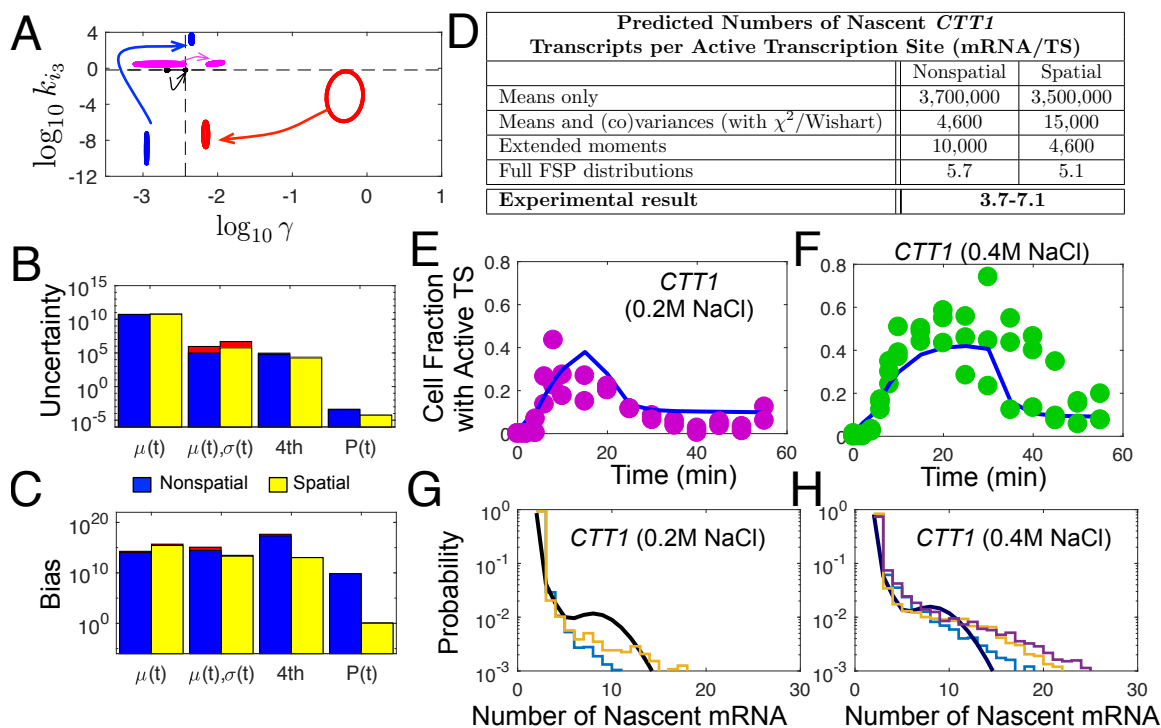
Figure S11: Overall bias and uncertainty quantification for *CTT1* transcription regulation. (A) Ninety percent confidence ellipses for the degradation rate (γ) and the maximal transcription initiation rate (k_{i3}) using the means only ($\mu(t)$, red), means and variances ($\mu(t), \sigma(t)$, blue), extended moment analyses (4th, magenta), or the full FSP distributions ($\mathbf{P}(t)$, black). Arrows show the effect of adding spatial information to the analysis. The dashed black lines show the baseline parameter combination corresponding to the best fit parameters for the spatial *CTT1* model. (B) Total uncertainty in parameters for the four methods. (C) Total parameter bias for the four methods. For B and C, the results for non-spatial and spatial analyses are shown in blue and yellow, respectively, and the red regions show the convergence of two independent MHA samples. (D) Prediction for the average number of nascent mRNA per active *CTT1* transcription site using each of the identified models. (E,F) Prediction for the fraction of cells with active *CTT1* TS versus time at (E) 0.2M NaCl and (F) 0.4M NaCl osmotic shock. (G,H) Model fit (black) and biological replicas (blue, orange, purple) for the distributions of nascent *CTT1* mRNA per TS.

31
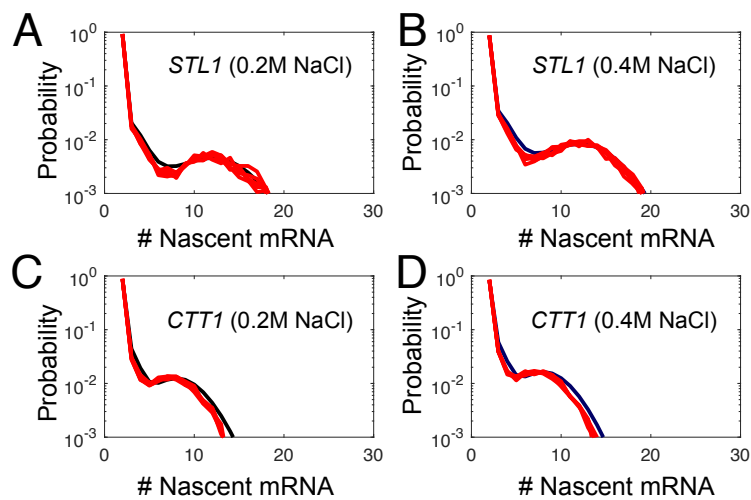
Figure S12: Comparison of FSP-based predictions (black) and several representative sets of 16,000 SSA simulations (red) for *STL1* TS intensity distributions following (A) 0.2M or (B) 0.4M NaCl osmotic shock and *CTT1* TS intensity distributions following (C) 0.2M or (D) 0.4M NaCl osmotic shock. The FSP and SSA analyses both use the best parameters found for the spatial FSP model (Table S3 for *STL1* and S4 for *CTT1*), with an elongation rate of 63nt/s.

CTT1 Probe Placement		STL1 Probe Placement	
Probe #	3' base relative to mRNA termination	Probe #	3' base relative to mRNA termination
1	1618	1	1630
2	1578	2	1604
3	1542	3	1577
4	1507	4	1546
5	1461	5	1518
6	1428	6	1493
7	1403	7	1449
8	1378	8	1389
9	1349	9	1364
10	1320	10	1325
11	1275	11	1282
12	1245	12	1250
13	1199	13	1200
14	1171	14	1172
15	1131	15	1144
16	1091	16	1104
17	1066	17	1078
18	1044	18	1035
19	1014	19	1001
20	987	20	971
21	953	21	913
22	913	22	884
23	884	23	856
24	854	24	830
25	832	25	805
26	810	26	768
27	788	27	743
28	743	28	702
29	693	29	670
30	671	30	635
31	648	31	610
32	615	32	574
33	591	33	545
34	568	34	509
35	546	35	472
36	519	36	435
37	491	37	396
38	468	38	356
39	445	39	324
40	390	40	287
41	313	41	250
42	289	42	223
43	237	43	184
44	166	44	138
45	105	45	113
46	57	46	86
47	27	47	59
48	0	48	24

Table S1: Locations for smRNA-FISH probes.

Osmotic Shock Condition	Parameter Values				
	r_1 (s^{-1})	r_2 (s^{-1})	η -	A -	M -
0.2M NaCl	6.1×10^{-3}	6.9×10^{-3}	5.9	9.3×10^9	2.2×10^{-2}
0.4M NaCl	6.1×10^{-3}	3.8×10^{-3}	5.9	9.3×10^9	2.2×10^{-2}

Table S2: Parameterization of the Hog1p nuclear enrichment signal at 0.2M and 0.4M NaCl osmotic shock.

STL1 Model Parameter Values – State Transition Rates								
Statistics	Spatial	$^*k_{12}$	$^*k_{21}^{(0)}$	$k_{21}^{(1)}$	$^*k_{23}$	$^*k_{32}$	$^*k_{34}$	$^*k_{43}$
[5]	No	1.3E+00	3.2E+03	7.7E+03	6.7E-03	2.7E-02	1.3E-01	3.8E-02
μ	No	1.2E-03 ± 7.9E-04	1.6E+01 ± 8.2E+00	5.4E+05 ± 2.7E+05	1.2E-03 ± 7.9E-04	1.1E-08 ± 2.9E-06	5.2E-03 ± 9.5E-05	2.6E-07 ± 2.8E-06
μ, Σ (χ^2)	No	1.4E-03 ± 2.7E-05	3.0E+01 ± 7.4E-01	9.7E+05 ± 2.3E+04	5.6E-03 ± 2.8E-04	7.5E-03 ± 6.2E-05	5.7E-05 ± 2.4E-05	8.7E-09 ± 3.5E-06
Extended Moments	No	5.6E-04 ± 2.5E-04	6.0E+02 ± 1.8E+02	7.3E+05 ± 1.7E+05	9.6E-04 ± 4.7E-04	4.2E-02 ± 3.3E-02	1.0E-08 ± 2.8E-06	4.4E-02 ± 2.5E-02
FSP	No	3.4E-03 ± 4.6E-05	5.1E+00 ± 9.3E-01	1.1E+03 ± 2.2E+02	6.4E-03 ± 9.6E-05	1.5E+00 ± 1.7E+00	8.3E+00 ± 9.2E+00	3.7E-02 ± 2.9E-03
μ	Yes	2.0E-03 ± 1.7E-04	2.6E+03 ± 4.1E+02	8.1E+05 ± 1.2E+05	1.1E-02 ± 2.1E-03	7.6E-03 ± 2.1E-03	8.6E-03 ± 5.2E-03	2.7E-02 ± 9.6E-03
μ, Σ (Wishart)	Yes	1.6E-03 ± 2.5E-05	3.9E+00 ± 1.0E-01	7.4E+04 ± 1.7E+03	5.7E-03 ± 2.2E-04	6.2E-02 ± 1.4E-03	1.0E-01 ± 4.7E-03	1.9E-02 ± 6.6E-04
Extended Moments	Yes	3.4E-03 ± 5.1E-04	8.2E+02 ± 1.2E+02	5.2E-04 ± 2.7E-05	7.6E-03 ± 1.6E-04	5.7E-03 ± 2.3E-04	3.5E-08 ± 9.9E-06	9.7E-03 ± 1.4E-03
FSP	Yes	2.6E-03 ± 2.6E-05	1.9E+01 ± 3.0E+00	3.2E+04 ± 5.1E+03	7.6E-03 ± 1.6E-04	1.2E-02 ± 2.8E-04	4.0E-03 ± 1.6E-04	3.1E-03 ± 8.9E-05

STL1 Model Parameter Values – Transcription and Degradation Rates							
Statistics	Spatial	$^*k_{i_1}$	$^*k_{i_2}$	$^*k_{i_3}$	$^*k_{i_4}$	$^\#\gamma$	t_0
[5]	No	7.8E-04	1.2E-02	9.9E-01	5.4E-02	4.9E-03	1.9E+02
μ	No	1.6E-02 ± 1.1E-02	1.5E+02 ± 1.2E+02	3.3E+02 ± 2.5E+02	3.7E-02 ± 3.6E-02	1.3E+00 ± 1.1E+00	3.4E+02 ± 1.7E+00
μ, Σ (χ^2)	No	2.6E+01 ± 1.5E+01	3.8E+04 ± 2.3E+04	1.6E+04 ± 1.0E+04	7.1E+02 ± 4.4E+02	5.2E+02 ± 3.2E+02	3.6E+02 ± 8.8E-01
Extended Moments	No	1.1E-04 ± 2.4E-05	3.9E-04 ± 8.8E-04	3.3E+01 ± 2.2E+01	2.1E+04 ± 2.4E+04	4.3E-03 ± 1.1E-04	1.0E+02 ± 4.7E+00
FSP	No	9.0E-05 ± 1.2E-05	2.0E-02 ± 7.7E-04	1.1E+02 ± 1.2E+02	4.1E-02 ± 1.4E-02	5.3E-03 ± 5.9E-05	2.0E+02 ± 2.3E+00
μ	Yes	2.0E-03 ± 1.1E-03	3.8E+00 ± 2.0E+00	1.5E-01 ± 3.1E-01	2.6E+01 ± 3.1E+01	4.5E-02 ± 6.2E-03	1.0E+00 ± 1.3E-01
μ, Σ (Wishart)	Yes	6.1E-01 ± 5.0E-02	1.1E+03 ± 5.2E+01	3.4E+03 ± 1.9E+02	1.9E-02 ± 2.6E-03	3.2E-02 ± 7.9E-04	8.9E-01 ± 2.1E-02
Extended Moments	Yes	1.2E-03 ± 4.3E-04	1.0E-01 ± 6.4E-02	1.8E+01 ± 5.9E+00	3.6E+03 ± 2.7E+03	2.4E-02 ± 2.5E-03	5.9E-01 ± 6.1E-02
FSP	Yes	5.9E-04 ± 2.6E-05	1.7E-01 ± 4.4E-03	1.0E+00 ± 1.4E-02	3.0E-02 ± 1.1E-03	8.3E-03 ± 1.0E-04	2.6E-01 ± 4.0E-03

STL1 Model Parameter Values – Spatial Rates				
Statistics	Spatial	$^\#\gamma_{\text{nuc}}$	$^\#\gamma_{\text{cyt}}$	$^\#k_{\text{transport}}$
μ	Yes	7.5E-01 ± 9.6E-01	4.5E-02 ± 6.2E-03	1.0E+00 ± 1.3E-01
μ, Σ (χ^2)	Yes	5.2E+02 ± 2.5E+01	3.2E-02 ± 7.9E-04	8.9E-01 ± 2.1E-02
Extended Moments	Yes	2.1E-01 ± 2.6E-01	2.4E-02 ± 2.5E-03	5.9E-01 ± 6.1E-02
FSP	Yes	2.2E-06 ± 2.0E-05	8.3E-03 ± 1.0E-04	2.6E-01 ± 4.0E-03

Table S3: Parameter values (and uncertainty) for the final model for *STL1*. Each parameter set was identified using a different fluctuation analysis: means (μ), means and (co)variances (μ and σ / Σ with χ^2 or Wishart formulation), the extended moments-based analysis using the means and covariances and a likelihood function defined by the first four moments, or distributions; and a different assumption on the spatial fluctuations: non-spatial or spatial). Parameter uncertainties were identified using the Metropolis Hastings algorithm on the corresponding likelihood function and are listed as plus or minus one standard deviation. Units of all parameters denoted by (*) are s^{-1}. Units of all parameters denoted by ($^\#$) are $Molecules^{-1}s^{-1}$. Units of $k_{21}^{(1)}$ are $AUC^{-1}s^{-1}$, where AUC is arbitrary units of Hog1p concentration. Units of t_0 are s.

				CTT1 Model Parameter Values – State Transition Rates				
Statistics	Spatial	$^*k_{12}$	$^*k_{21}^{(0)}$	$k_{21}^{(1)}$	$^*k_{23}$	$^*k_{32}$	$^*k_{34}$	$^*k_{43}$
[5]	No	1.3E+00	3.2E+03	7.7E+03	1.9E-02	1.8E-02	1.3E-01	8.3E-03
μ	No	2.5E-05 ± 2.3E-05	2.0E+03 ± 1.2E+03	3.8E+04 ± 2.1E+04	2.6E-04 ± 2.3E-04	3.0E-03 ± 8.7E-04	8.2E-04 ± 3.3E-04	1.8E-03 ± 6.2E-04
μ, Σ (χ^2)	No	1.9E-03 ± 2.9E-05	7.1E-02 ± 9.5E-04	5.9E+00 ± 4.8E-01	5.3E-07 ± 6.8E-06	3.4E-03 ± 1.2E-03	3.1E-06 ± 7.7E-06	2.5E-03 ± 5.6E-04
Extended Moments	No	7.2E-04 ± 5.2E-04	7.6E+02 ± 2.0E+02	2.9E+03 ± 6.6E+02	1.4E-03 ± 8.2E-04	1.4E-03 ± 5.2E-04	6.1E-08 ± 5.9E-06	6.1E-03 ± 1.5E-03
FSP	No	3.8E-03 ± 4.9E-05	2.3E-01 ± 9.6E-03	3.5E+00 ± 3.7E-01	5.0E-03 ± 1.1E-04	4.0E-03 ± 1.2E-04	9.4E-03 ± 8.4E-04	4.4E-03 ± 3.1E-04
μ	Yes	7.2E-06 ± 1.0E-05	1.6E+03 ± 7.2E+02	3.8E+03 ± 1.7E+03	1.5E-03 ± 2.1E-04	1.3E-03 ± 1.6E-04	2.1E-04 ± 9.3E-05	2.5E-03 ± 2.6E-04
μ, Σ (Wishart)	Yes	1.5E-03 ± 1.6E-05	1.5E-01 ± 3.3E-03	1.2E+02 ± 4.3E+00	9.2E-04 ± 4.2E-05	3.8E+00 ± 1.7E+00	4.2E+02 ± 1.8E+02	1.0E-01 ± 8.5E-03
Extended Moments	Yes	1.7E-04 ± 2.4E-05	2.7E+00 ± 1.0E+00	3.3E+03 ± 1.3E+03	3.1E-03 ± 5.2E-05	7.5E-04 ± 5.7E-05	5.3E-04 ± 1.4E-04	2.2E-01 ± 6.5E-02
FSP	Yes	2.1E-03 ± 2.2E-05	9.2E-03 ± 2.1E-04	2.7E+03 ± 4.1E+02	3.1E-03 ± 5.2E-05	7.4E-03 ± 1.7E-04	5.6E-04 ± 2.6E-05	1.0E-07 ± 1.5E-05

			CTT1 Model Parameter Values – Transcription and Degradation Rates				
Statistics	Spatial	$^*k_{i_1}$	$^*k_{i_2}$	$^*k_{i_3}$	$^*k_{i_4}$	$^\#\gamma$	t_0
[5]	No	6.2E-04	9.8E-03	1.0E+00	1.6E-03	2.0E-03	1.9E+02
μ	No	2.6E-01 ± 6.4E-02	2.2E+03 ± 1.3E+03	4.7E-03 ± 3.6E-03	4.2E+05 ± 2.3E+05	5.5E-01 ± 1.4E-01	2.6E+02 ± 4.0E+00
μ, Σ (χ^2)	No	6.3E-05 ± 1.0E-04	2.1E-01 ± 1.8E-03	2.4E-08 ± 6.8E-06	5.2E+02 ± 3.1E+02	1.1E-03 ± 1.3E-05	2.6E+02 ± 1.6E+00
Extended Moments	No	3.3E-03 ± 7.9E-04	6.2E-08 ± 5.9E-06	3.1E+00 ± 6.8E-01	1.2E+03 ± 3.1E+02	1.9E-03 ± 6.4E-04	4.9E+01 ± 1.3E+01
FSP	No	1.1E-03 ± 3.9E-05	9.9E-02 ± 2.7E-03	6.1E-01 ± 1.9E-02	2.4E-02 ± 3.8E-03	2.1E-03 ± 3.8E-05	2.1E+02 ± 2.1E+00
μ	Yes	1.1E-01 ± 3.5E-02	4.4E+03 ± 2.8E+03	1.5E-07 ± 4.1E-07	4.0E+05 ± 2.3E+05	6.9E-03 ± 2.6E-04	3.0E-01 ± 1.0E-02
μ, Σ (Wishart)	Yes	3.1E-03 ± 2.1E-04	4.6E-01 ± 1.1E-02	1.7E+03 ± 7.3E+02	1.6E-02 ± 1.4E-02	4.5E-03 ± 9.0E-05	2.6E-01 ± 3.9E-03
Extended Moments	Yes	5.6E-03 ± 5.8E-04	6.7E+00 ± 1.4E+00	3.5E+00 ± 6.4E-01	5.2E+02 ± 1.3E+02	9.4E-03 ± 1.0E-03	3.8E-01 ± 3.5E-02
FSP	Yes	2.5E-03 ± 5.0E-05	1.2E-01 ± 1.8E-03	6.5E-01 ± 8.6E-03	5.5E-04 ± 9.2E-05	3.7E-03 ± 4.2E-05	1.8E-01 ± 2.4E-03

		CTT1 Model Parameter Values – Spatial Rates		
Statistics	Spatial	$^\#\gamma_{\mathrm{nuc}}$	$^\#\gamma_{\mathrm{cyt}}$	$^\#k_{\mathrm{transport}}$
μ	Yes	4.9E+00 ± 1.7E+00	6.9E-03 ± 2.6E-04	3.0E-01 ± 1.0E-02
μ, Σ (χ^2)	Yes	4.2E-03 ± 4.5E-03	4.5E-03 ± 9.0E-05	2.6E-01 ± 3.9E-03
Extended Moments	Yes	6.8E-07 ± 2.2E-06	9.4E-03 ± 1.0E-03	3.8E-01 ± 3.5E-02
FSP	Yes	1.0E-07 ± 1.5E-05	3.7E-03 ± 4.2E-05	1.8E-01 ± 2.4E-03

Table S4: Parameter values (and uncertainty) for the final model for *CTT1*. Each parameter set was identified using a different fluctuation analysis: means (μ), means and (co)variances (μ and σ/Σ with χ^2 or Wishart formulation), the extended moments-based analysis using the means and covariances and a likelihood function defined by the first four moments, or distributions computed with the FSP approach; and a different assumption on the spatial fluctuations: non-spatial or spatial). Parameter uncertainties were identified using the Metropolis Hastings algorithm on the corresponding likelihood function and are listed as plus or minus one standard deviation. Units of all parameters denoted by (*) are s^{-1}. Units of all parameters denoted by ($^\#$) are $Molecules^{-1}s^{-1}$. Units of $k_{21}^{(1)}$ are $AUC^{-1}s^{-1}$, where AUC is arbitrary units of Hog1p concentration. Units of t_0 are s.

STL1 **Relative -Log$_{10}$-Likelihood Values**					
		Likelihood Function			
Fitting Data	Spatial	$\boldsymbol{\mu}^*$	$\boldsymbol{\mu}$ and $\boldsymbol{\Sigma}^*$	Extended Moments*	Distributions
Means only	No	0	-1.72E+04	-1.64E+04	-6.97E+04
Means and variances (chi^2)	No	-4.46E+02	0	-1.85E+04	-6.26E+04
Extended moments	No	-6.83E+02	-3.71E+04	0	-4.94E+04
Full FSP Distributions	No	-2.75E+03	-1.45E+04	-6.64E+02	0
Means only	Yes	0	-6.46E+04	-7.32E+03	-2.72E+04
Means and variances (Wishart)	Yes	-7.62E+02	0	-7.20E+03	-1.77E+04
Extended moments	Yes	-1.88E+03	-4.75E+04	0	-8.15E+04
Full FSP Distributions	Yes	-1.03E+04	-2.40E+04	-3.45E+03	0
CTT1 **Relative -Log$_{10}$-Likelihood Values**					
		Likelihood Function			
Fitting Statistics	Spatial	$\boldsymbol{\mu}^*$	$\boldsymbol{\mu}$ and $\boldsymbol{\Sigma}^*$	Extended Moments*	Distributions
Means only	No	0	-1.83E+05	-1.48E+03	-3.62E+05
Means and variances (chi^2)	No	-1.61E+03	0	-2.29E+03	-3.06E+04
Extended moments	No	-9.49E+02	-5.24E+04	0	-9.39E+04
Full FSP Distributions	No	-4.76E+03	-5.62E+03	-1.83E+03	0
Means only	Yes	0	-3.85E+05	-1.94E+03	-3.57E+05
Means and variances (Wishart)	Yes	-3.11E+03	0	-1.94E+04	-2.45E+04
Extended moments	Yes	-4.13E+03	-1.25E+05	0	-2.36E+05
Full FSP Distributions	Yes	-1.56E+04	-1.60E+04	-6.65E+03	0

Table S5: Relative log-likelihood values for different likelihoods that compare the means ($\boldsymbol{\mu}$), means and (co)variances ($\boldsymbol{\mu}$ and $\boldsymbol{\sigma}/\boldsymbol{\Sigma}$ with χ^2 or Wishart formulation), the extended moments-based approach, or full distributions. Each row corresponds to a different combination of gene and identification strategy. Each column corresponds to a different likelihood function. Values presented are $\log_{10}$ of the actual likelihoods relative to the best value found for that objective function. For example, a value of zero states that the corresponding parameter set (Tables S4,S3) maximizes that likelihood function. A value $-x_{ij}$, in the i-row and j-column states that the parameters identified using the ith likelihood yields $10^{x_{ij}}$-fold worse fit to the jth likelihood function. See Section 2.8 for detailed instructions on how to interpret this table. *The moment-based likelihood functions are approximated using the Central Limit Theorem as discussed in the Materials and Methods.

Estimation of *CTT1* Transcription Elongation Rates (Nt/s)			
Analysis	**Spatial**	**Simplified Theory**	**Detailed FSP**
Means only	No	5.93E+07$\pm$ 5.9E+06	N/A
Means and variances (χ^2)	No	7.25E+04$\pm$ 7.3E+03	N/A
Extended moments	No	1.65E+05$\pm$ 1.7E+04	N/A
Full FSP Distributions	No	85.8$\pm$8.6	45$\pm$ 14
Means only	Yes	5.54E+07 $\pm$ 5.6E+06	N/A
Means and (co)variances (Wishart)	Yes	2.39E+05 $\pm$ 2.4E+04	N/A
Extended moments	Yes	7.27E+04$\pm$ 7.3E+03	N/A
Full FSP Distributions	Yes	91.2$\pm$ 9.1	*$\mathbf{63\pm13}$

Table S6: Elongation rates identified for *CTT1* transcription using the best parameters identified in Tables S4 and the measured TS intensity data. For each case – means ($\boldsymbol{\mu}$), means and (co)variances ($\boldsymbol{\mu}$ and $\boldsymbol{\Sigma}$), extended moments, or distributions – we present the upper bound on the rates using the simplified theoretical model and the more precise rates using the detailed FSP-TS analysis, when possible. Uncertainty in these rates is given as the standard error of the mean computed from the five biological replicates. (*Figs. 1D, 4D, and S11 use the rate identified from *CTT1* TS intensity measurements and the corresponding fit of the elongation rate with the spatial FSP analysis.)